E.L. Moreland[1], R.E. Arvidson[2, 3], R.V. Morris[4], T. Condus[2, 3], M.N. Hughes[2, 3], C.M. Weitz[5], and S.J. VanBommel[2, 3]

[1]Department of Earth, Environmental, and Planetary Sciences, Rice University, Houston, TX.

[2]Department of Earth and Planetary Sciences, Washington University in St. Louis, St. Louis, MO.

[3]McDonnell Center for the Space Sciences, Washington University in St. Louis, St. Louis, MO.

[4]ARES, NASA Johnson Space Center, Houston, TX.

[5]Planetary Science Institute, Tucson, AZ.

Draft for Journal of Geophysical Research: Planets

06/21/22

Corresponding author: Eleanor Moreland (morelandellie@rice.edu)

Key Points:

- Orbital and in-situ data show variation between the basaltic sands that dominate the active Bagnold dunes and Sands of Forvie sand sheet.
- The two deposits are separated by ~2.5 kilometers, so this variation is relevant to interpretation of aeolian transport processes on Mars.
- The variation is interpreted to result from unconstrained dune migration versus topographically inhibited migration for the sand sheet.

Abstract

The Bagnold linear dune field investigated by *Curiosity* at Mount Desert Island (MDI) is in Gale crater, north of the ~5.5 km high Aeolis Mons mound. False-color images (RGB, 2.496, 1.802, and 1.235 µm, respectively) generated from Mars Reconnaissance Orbiter (MRO) Compact Reconnaissance Imaging Spectrometer for Mars (CRISM) data show the dune field has a reddish-brown color. A sand sheet located south of the Bagnold dunes, the Sands of Forvie (SoF), is darker and lacks the reddish-brown color. Single scattering albedo (SSA) spectra retrieved at 12 m/pixel using along-track oversampled CRISM observation FRT00021C92 show a long wavelength (1.7 to 2.5 µm) rise for the MDI dunes. Over the same wavelength interval, SoF is characterized by a broad ~2.2 µm absorption feature, consistent with color differences between the two deposits. Checkerboard unmixing of the SSA image cube isolated spectral endmembers within the MDI and SoF. Nonlinear modeling using Hapke (2012) theory implies finer grain sizes for MDI compared to SoF, with inferred abundances of basaltic glass > feldspar > olivine > pigeonite > augite for MDI, and basaltic glass

> feldspar > augite > olivine for SoF. These results are similar for the mean spectra of each region and coincide with *Curiosity*-based observations that MDI contains smaller ripples with overall finer grains, while SoF has large megaripples and concentrated coarser grains on the crests. Although these deposits are only located ~2.5 kilometers away from one another, wind and local topographic controls influence their grain size and mineralogy.

Plain Language Summary

In Gale Crater, both the Mount Desert Island (MDI) area within the Bagnold dune field and the Sands of Forvie (SoF) deposit located to the south of Glen Torridon have been shown, using Curiosity rover data, to consist of basaltic materials. We employed along-track oversampled CRISM hyperspectral image data (0.50 to 2.6 µm) covering these areas and processed images to retrieve surface spectra free of the influence of atmospheric aerosols and gases. Non-linear modeling of the spectra on a pixel-by-pixel basis shows that spectral differences between the two sand sheets are a consequence of differences in glass and pigeonite contents, together with coarser grains in the Sands of Forvie deposit. Results are consistent with wind-induced preferential migration of finer grains up onto the Greenheugh pediment for SoF, as opposed to the uninhibited downwind migration of the MDI sands. Results are also relevant to understanding wind-blown sand deposits in the Martian rock record, considering that the two sand deposits are located only ~2.5 kilometers from one another, yet have different characteristics that are a consequence of local topographic controls.

1 Introduction

The Mars Science Laboratory (MSL) rover *Curiosity* has explored the northwestern floor of Gale crater and its central ~5.5 km tall mound, Aeolis Mons (informally named Mount Sharp), focusing on investigating exposed strata to infer past environments of deposition and overall potential for ancient habitability (Grotzinger et al., 2012, 2015; Vasavada et al., 2014; Bennett et al., 2022; and references therein). The local radiation environment, atmospheric dynamics, and the nature of modern sand deposits have also been investigated (e.g., Vasavada et al., 2014 and references therein). Sand measurements using *Curiosity*'s instrument payload have been conducted at multiple locations, largely focusing on the Bagnold dune field to the north of Mount Sharp (e.g., Bridges & Ehlmann et al., 2018; Lapotre & Rampe, 2018; Figure 1). In-situ data from the sands have also been used synergistically with Mars Reconnaissance Orbiter (MRO) Compact Imaging Spectrometer for Mars (CRISM; Murchie et al., 2007) observations to extend interpretations of the nature of the dunes from the relatively small areas characterized by the rover to larger regions covered by hyperspectral imaging data (e.g., Lapotre et al., 2017a; Rampe et al., 2018). Within the Bagnold dune field, observations at the Namib barchan dune and at the Nathan Bridges and Mount Desert Island (MDI) linear dune deposits were made (Lapotre & Rampe, 2018). On Mt. Sharp, *Curiosity*-based measurements were acquired at the northern edge of the Sands of Forvie (SoF) sand sheet located on the southern edge of Glen Torridon (Weitz et al., 2022; Sullivan et al., 2022; Figure 1).

In this paper we extend the synergistic and comparative analyses of *Curiosity* and CRISM-based data sets to include *Curiosity*'s southern Bagnold dune measurements (MDI area) and the SoF sand sheet. We utilize CRISM along-track oversampled observation (ATO) FRT00021C92 which covers both sites to add orbital perspectives to the analyses.

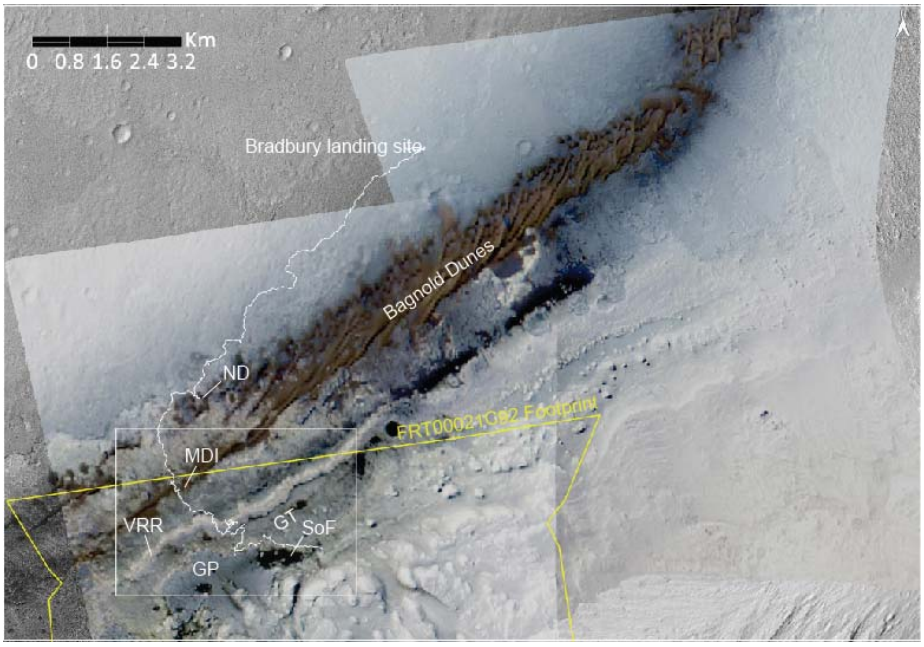

Figure 1. Two CRISM false color images overlain onto a HiRISE image mosaic. *Curiosity*'s traverses from the Bradbury Landing Site to sol 3052 at the base of Mont Mercou are shown. The CRISM data RGB band center wavelengths are 2.496, 1.802, and 1.237 µm, respectively. The reddish-brown color of the Bagnold dune field as opposed to the darker, less red sand fields to the southeast is a consequence of the increased reflectance with increasing wavelength for the Bagnold dune deposits as opposed to the deposits located to the southeast. The white box delineates the location of the detailed study area (Figure 3) and the yellow lines show the outline of CRISM along-track oversampled scene FRT00021C92, the focus of this paper. The footprints of CRISM scenes HRL0000BABA (left) and FRT0000C518 (right) are also shown. VRR stands for Vera Rubin ridge, GT for Glen Torridon, and GP for Greenheugh pediment. NB stands for the Namib barchan dune, MDI stands for Mount Desert Island, and SoF for Sands of Forvie. In this paper we focus on comparisons of results for MDI and SoF areas, which have distinctly different color and thus spectral properties. CRISM data have been processed to single scattering albedo (SSA), as described in Section 2 of the text.

We first review previous rover- and orbital-based results for the Bagnold dunes, with a focus on the MDI location within the linear Bagnold dunes and results

from *Curiosity*'s measurements on the northern edge of the SoF sand sheet. The CRISM ATO observation (Figures 2 and 3) is then used to retrieve single scattering albedo (SSA) spectra from 0.50 to 2.6 µm at 12 m/pixel scale, i.e., a high enough spatial resolution to properly sample both the MDI and SoF sand deposits. The Bagnold linear dunes, including MDI, show a reddish-brown color, whereas the southern sand deposits, including SoF, are darker and lack the reddish-brown color (Figures 1-3). We employed CRISM spectra to determine the reasons for these color differences, focusing on retrieval of mineral abundances and grain sizes for these two deposits.

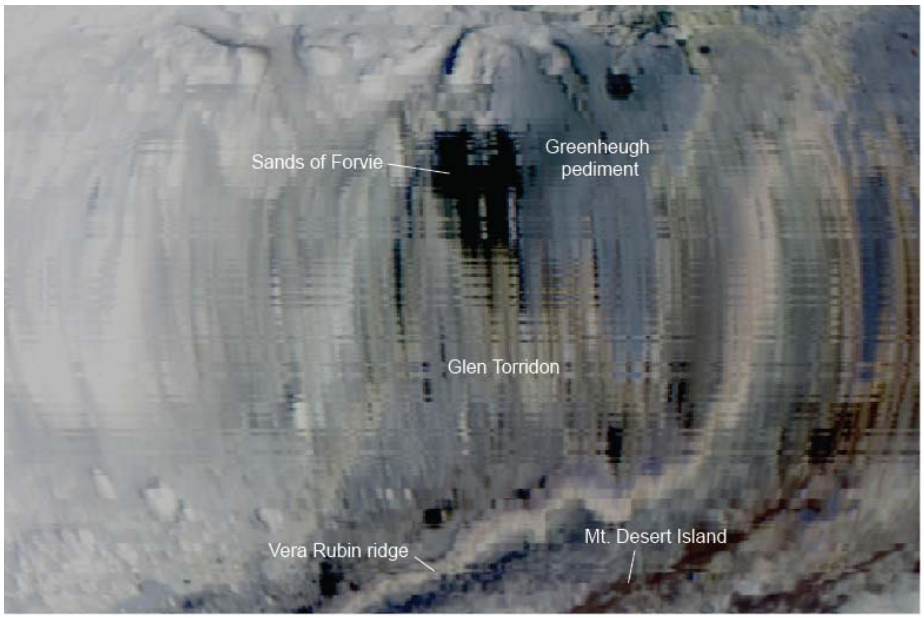

Figure 2. Sensor space CRISM scene FRT00021C92 false color view is shown with the same RGB wavelengths as shown for the CRISM data in Figure 1. North is to the bottom of the figure. CRISM data are in SSA units. Key features are labeled to show the high degree of along track overlap in the center of the scene that is a consequence of explicitly commanding this gimbaled line scanning hyperspectral imaging system to obtain repeated coverage of the same locations. The overlap permits regularization of the intrinsic 18 m/pixel data to 12 m/pixel in map projected space.

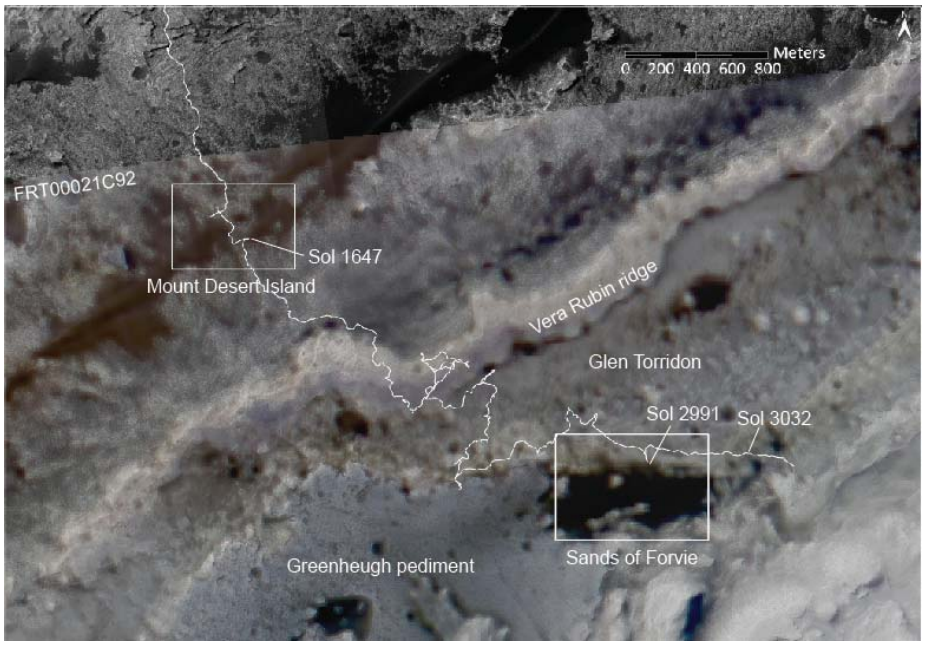

Figure 3. FRT00021C92 regularized and map projected data overlain with 50% transparency on the HiRISE red image mosaic using the RGB assignments delineated in the caption for Figure 1. CRISM data are in SSA units. White boxes delineate locations that include *Curiosity*'s stop for sand-based measurements. These areas are shown using color HiRISE data in Figures 4 and 7. Sols 1647 and 2991 correspond to times when *Curiosity* acquired Mastcam image data of the sand deposits as shown in Figures 5, 6, 8, and 9.

2 Summary of Previous Results

Three orbital instruments have been used to infer the mineralogy of the Bagnold dunes. The Mars Global Surveyor's Thermal Emission Spectrometer (TES) acquired data interpreted to indicate the dominance of ferrous silicate minerals, thereby pointing to a basaltic source (Lane & Christensen, 2013). Rogers and Bandfield (2009) reported similar results using a combination of TES and Mars Odyssey's Thermal Emission Infrared Imaging System (THEMIS). Seelos et al. (2014), using CRISM data projected to 18 m/pixel and covering the northern part of the Bagnold dunes, inferred that the Bagnold barchan dunes exhibit an enhanced olivine spectral signature as compared to an enhanced pyroxene signature for the linear dunes. Edwards et al. (2018) inferred sand-sized particles (0.11 to 0.35 mm) for the Namib dune area within the Bagnold complex from Curiosity and THEMIS data. In summary, orbital data indicate that the Bagnold dunes are dominated by sand sized particles associated with ferrous silicate minerals and glass, i.e., basaltic sands. Bennett et al. (2018) employed THEMIS and two CRISM scenes projected at 18 m/pixel to investigate color and spectral reflectance variations between the Bagnold dunes and a sand sea

located in the western part of Gale crater, farther west than the deposits in this study. They concluded that the color and spectral properties of the western sand sea were likely influenced by dust cover as compared to the Bagnold dunes, yet they discussed and did not rule out variations due to grain size sorting.

CRISM-based SSA spectral data were employed by Kreisch et al. (2017) to infer mineralogy and grain sizes using Hapke (2012) non-linear modeling for along-track oversampled (ATO) scene ATO0002EC79 covering the Namib dune area. They concluded that the mineral abundance and grain size retrievals were compatible with the Gobabeb sand sample from within the Bagnold dune complex measured by *Curiosity*'s Chemistry and Mineralogy (CheMin) X-ray diffraction instrument (Achilles et al., 2017). Nonlinear modeling of the CRISM dune spectra retrieved abundances in decreasing order of amorphous material, olivine, plagioclase, pyroxene, and magnetite. This work was followed by a more extensive analysis of CRISM data covering the Bagnold dunes that showed minerals are spatially distributed and concluded that nonlinear modeling results should be viewed in a strict statistical sense to understand how well the results are constrained by the available endmembers and the spectral characteristics of CRISM input spectra (Lapotre et al., 2017a, 2017b). Rampe et al. (2018) included both CheMin and CRISM data in their analyses of Gobabeb (Namib dune sample) and Ogunquit Beach (MDI dune sample). The CheMin results showed the presence of XRD-amorphous material in addition to plagioclase, olivine, augite, and pigeonite, in decreasing order of abundance for both Gobabeb and Ogunquit Beach. CRISM SSA spectra retrieved from scene HRL0000BABA at 12 m/pixel in the MDI area were modeled using Hapke (2012) theory in their paper. Model results indicated abundances ranked in decreasing order as plagioclase, an amorphous phase, augite, olivine, pigeonite, and magnetite. The authors emphasized caution when drawing direct comparisons between CRISM data and CheMin, resulting from differences in the nature of the instruments and the data they acquire. For example, CRISM spectral radiances sample only micrometers into surface materials and are averages over areas tens of meters square, whereas CheMin analyzes a small volume (~10 mm^3) of scooped sand with a grain size <0.15 mm (Blake et al., 2012).

Ehlmann et al. (2017, and references therein) provided an extensive summary of measurements acquired by *Curiosity* for the northern Bagnold dunes, specifically Namib and High dunes. The sands range in grain size from 0.045 to 0.5 mm, are loose, rounded, variably colored, and have significant fractions of an amorphous component. Plagioclase, olivine, and pyroxenes comprise the vast majority of the crystalline phases. Weitz et al. (2018, 2022) continued the analysis of sand deposits using *Curiosity* data, including sands found along the traverse between the Vera Rubin ridge to SoF. They found that 0.050 to 0.150 mm grains dominate active sand deposits, with much coarser grains (1-2 mm) coming from weathering of local bedrock. Christian et al. (2022) used CRISM ATO FRT00021C92 to derive apparent thermal inertias for the Bagnold dunes in the MDI area and found that values were lower than what was found for the SoF deposit, implying that SoF was dominated by larger grains. Sullivan et

al. (2022) examined ripple orientations for sand deposits in Glen Torridon and inferred sand-driving winds moved toward the southwest.

3 Data and Methods

Five groups of data were utilized in the analyses presented in this paper. CRISM scenes HRL0000BABA and FRT0000C518 were used to provide an overview of the sand deposits within the vicinity of *Curiosity*'s traverses (Figure 1). CRISM ATO FRT00021C92 was employed to identify and map mineral phases within MDI dune field and the SoF sand sheet. The mapping included spectral ranges for CRISM short wavelength (S) and long wavelength (L) data cubes after retrieving surface SSA spectra, as discussed below. An MRO High Resolution Imaging Science Experiment (HiRISE) mosaic (McEwen et al., 2007) covering the same regions as the CRISM data was also utilized (Calef & Parker, 2016). These data were further complemented by *Curiosity*'s Navcam (Maki et al., 2012), Mastcam (Bell et al., 2017), the Mars Hand Lens Imager (MAHLI; Edgett et al., 2012), and the Mars Descent Imager (MARDI; Malin et al., 2017) image data acquired at the MDI and SoF sand deposits (Table 1). Compositionally, the Alpha Particle X-ray Spectrometer (APXS; Gellert & Clark, 2015) provides a means to evaluate the hypothesis that disaggregated bedrock grains mix with basaltic sands at the margins of both the MDI and SoF basaltic sand deposits.

Table 1. Reference information for data used in manuscript.

Instrument/Data	PDS (Planetary Data System) product ID	DOI
High Resolution Imaging Science Experiment (HiRISE)	[ESP_024234_1755, ESP_024300_1755, PSP_009650_1755, PSP_009716_1755, PSP_010573_1755, PSP_010639_1755, PSP_009505_1755, PSP_009571_1755, ESP_011417_1755, ESP_011562_1755, ESP_018854_1755, ESP_018920_1755, ESP_023957_1755, ESP_024023_1755, ESP_024102_1755, ESP_025368_1755, PSP_009149_1755, PSP_009294_1755, ESP_012551_1755, ESP_012841_1755, PSP_001488_1755, PSP_001752_1755, ESP_019698_1755, ESP_019988_1755] (Calef & Parker, 2016 MSL Gale Merged Orthophoto Mosaic)	/1520179 10.17189/1520303
Compact Reconnaissance Imaging Spectrometer for Mars (CRISM)	FRT00021C92 HRL0000BABA FRT0000C518	/1519470
Navigation Camera (NavCam)	N_L000_3032_ILT086CYP_1520356_UNCORM1	/1520356
Mast Camera (Mastcam)	Imaging sequence mcam08525 (Fig. 5) Imaging sequence mcam08533 (Fig. 6) Imaging sequence mcam15588 (Fig. 8) Imaging sequence mcam15622 (Fig. 9) Imaging sequence mcam15825 (Fig. 10)	/1520328 Credit: NASA/JPL-Caltech/MSSS

Instrument/Data	PDS (Planetary Data System) product ID	DOI
Mars Descent Imager (MARDI)	3032MD0011410000202527[illegible]	/2012JE004CX Credit: NASA/JPL-Caltech/MSSS
Mars Hand Lens Imager (MAHLI)	3036MH0001530001100787[illegible] 3036MH0001530001100789[illegible] 3036MH0001530001100791[illegible]	/2012JE004CX Credit: NASA/JPL-Caltech/MSSS
Alpha Particle X-Ray Spectrometer (APXS)	APB_666970610RWP30360[illegible] APB_666950991RWP30350861456_____P1	/2012JE004CX /3614767_____P1
Modeling Code	n/a	/2016JE005248
All synthetic glasses[a]	n/a	/2jv6-c769
Labradorite laboratory sample[b]	n/a	/1519032
Olivine laboratory sample[b]	n/a	/ds1035 10.1029/JB092iB11p11457
Pigeonite laboratory sample[b]	n/a	/Z0QN652C
Augite laboratory sample[b]	n/a	/j.1945-5100.2010.01158.x

[a]See Table S1 for chemical compositions.
[b]See Table S2 for chemical compositions.

We specifically used log ratio values of compositions in a correspondence analysis (Aitchison, 1994) to reduce the dimensionality of the compositional data sets to explore the extent of regolith contributions to the sand measurements. The final data set consisted of laboratory-based spectra used in the Hapke (2012) modeling of mineral assemblages to retrieve phase abundances and grain sizes (Tables 1 and 2).

SSA spectra were retrieved from both the S and L CRISM data (Murchie et al., 2007). The processing included explicit modeling of atmospheric gases and aerosols using the DISORT radiative code (Stamnes et al., 1988; Wolff et al., 2009) adapted for Mars conditions and the Hapke photometric function (Hapke, 2012) as a surface boundary condition (Arvidson et al., 2006). SSA spectral cubes were regularized, and the best estimate of surface spectral properties were retrieved in the presence of Poisson noise using a log maximum likelihood approach (MLM) and projected at 12 m/pixel (Kreisch et al., 2017; He et al., 2019). Comparison of the sensor space view shown in Figure 2 with the map projected view shown in Figure 3 demonstrates the effectiveness of this processing pipeline for our two sand deposit study sites (MDI and SoF). Both the S and L 12 m/pixel processed data cubes for FRT00021C92 were registered to the 25 cm/pixel HiRISE mosaic. The separate S and L data cubes were also joined

to retrieve full VNIR spectra from 0.50 to 2.60 µm.

CRISM SSA spectra are a representation of a mixture of minerals and amorphous phases at varying abundances and grain sizes. Two techniques were used to infer sand mineralogy, spectrally speaking. First, the Sequential Maximum Angle Convex Cone (SMACC) endmember model (Gruninger et al., 2004) was used to delineate endmember spectra for regions of interest (ROIs) for both sand deposits. The procedure was used to choose endmember spectra from the scene and then model each pixel within the sand deposit as a linear combination of endmembers. This approach helped to evaluate the spectral heterogeneity of the sands. Second, we retrieved mineral phase abundances and grain sizes using the Hapke (2012) model and laboratory spectra (Table 2). We employed a Bayesian implementation of the Hapke model using a Markov chain Monte Carlo (MCMC) algorithm as developed by Lapotre et al. (2017b). The MCMC algorithm produced a variety of best fit spectra over ranges of abundances and grain sizes, and thus we employed violin plots (Hintze & Nelson, 1998) to show the statistical distribution of fits for numerous runs. The runs were conducted on two representative CRISM spectral endmembers identified by the SMACC method, chosen to avoid bedrock regolith contributions to the ferrous silicates within the sand deposits and thereby making model retrievals more robust.

Table 2. Reference information for model endmembers.

Endmember[a]	Specimen ID	Composition	Average Grain Size of sample (µm)	Density (kg/m^3)	R
Labradorite	DH-CMP-016	An_{62}	15	2690	1
GMS_Gl	N/A	See Table S1	68	2780	1
Olivine	Olivine_KI3188	Fo_{51}	25	3320	1
Augite	DL-CMP-071-A	$Wo_{46}En_{23}Fs_{31}$	75	3400	1
Pigeonite	DL-CMP-012-A	$Wo_3En_{62}Fs_{35}$	75	3380	1

[a]See Table 1 for reference information.

4 The View from HiRISE and Curiosity

Mount Desert Island: The MDI sand deposit is located on a linear dune that is part of the overall Bagnold dune complex (Figure 1). It is located north of where *Curiosity* traversed through a narrow dune gap, with the MDI dune located to the northeast of the traverse and the Nathan Bridges dune to the southwest (Figure 4).

Figure 4. Portion of the HiRISE color mosaic centered on the Bagnold dunes region investigated by *Curiosity*. The linear dunes are evident extending from NE to SW. The white line delineates the path taken by *Curiosity*, including the stop at Mount Desert Island for detailed sand-based measurements.

Both dune segments exhibit the relatively reddish-brown color seen in CRISM for the linear dunes that dominate the Bagnold dunes (Figures 1-3). The surfaces of both the MDI and Nathan Bridges dunes have wind-blown cm-high ripples (Silvestro et al., 2013; Lapotre et al., 2018; Figure 5). The key stop for dune measurements began on sol 1647 when *Curiosity* was commanded to analyze and acquire a sand sample at the edge of the MDI dune for analysis by CheMin (Blake et al., 2012; Lapotre & Rampe, 2018).

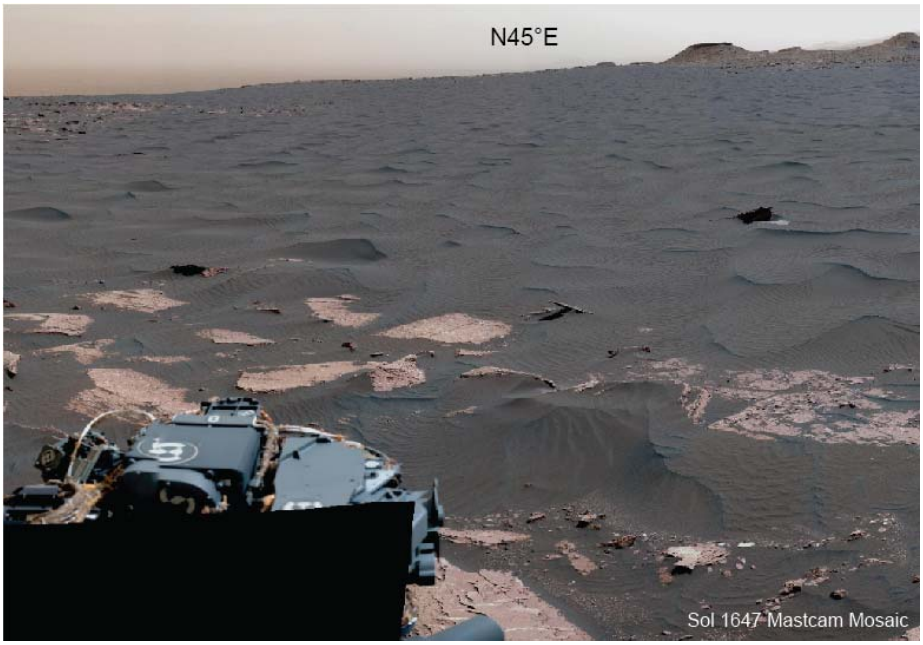

Figure 5. Portion of a Mastcam color mosaic taken on sol 1647 at Mount Desert Island looking to the northeast along the linear Bagnold dunes. Platy bedrock is evident in the foreground. Number at the top of the figure denotes azimuthal direction measured clockwise from north. Image credit: NASA/JPL-Caltech/MSSS.

An extensive imaging and APXS measurement campaign focused on this sample, named Ogunquit Beach. A left wheel scuff into the edge of MDI demonstrated that the sands are slightly cohesive and break into small clods (Figure 6). In the wavelengths covered by Mastcam color images (RGB 0.640, 0.554, 0.495 µm; Bell et al. 2012) the deposits exhibit a relatively reddish-brown surface color, with darker sands underneath (Figure 6). Analysis of Mastcam multispectral data showed that the interior deposits are dominated by ferrous silicate minerals (Johnson et al., 2018). A CheMin sample was acquired by scooping several centimeters into the sand deposit and delivering a portion sieved to <0.15 mm to the instrument. As discussed in Section 2, CheMin data showed the presence and abundance of amorphous and ferrous silicate phases.

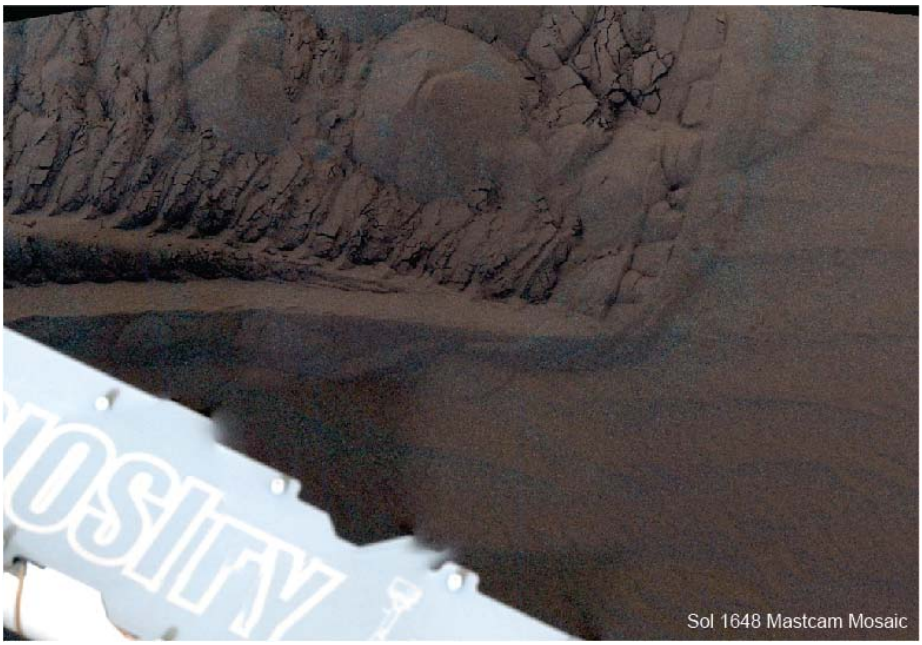

Figure 6. Portion of a Mastcam color mosaic showing the imprint of the left front wheel in the dune sands. The dune sand is slightly cohesive and exhibits as reddish tint. Data acquired on Sol 1648 during *Curiosity*'s Mount Desert Island campaign. Image credit NASA/JPL-Caltech/MSSS.

Sands of Forvie: SoF is a sand sheet that is located just to the south of Glen Torridon, with its west side bordered by the eastern scarp of the Greenheugh pediment and the southern extent bounded by topographic relief associated with Mount Sharp (Figures 1, 3, 7).

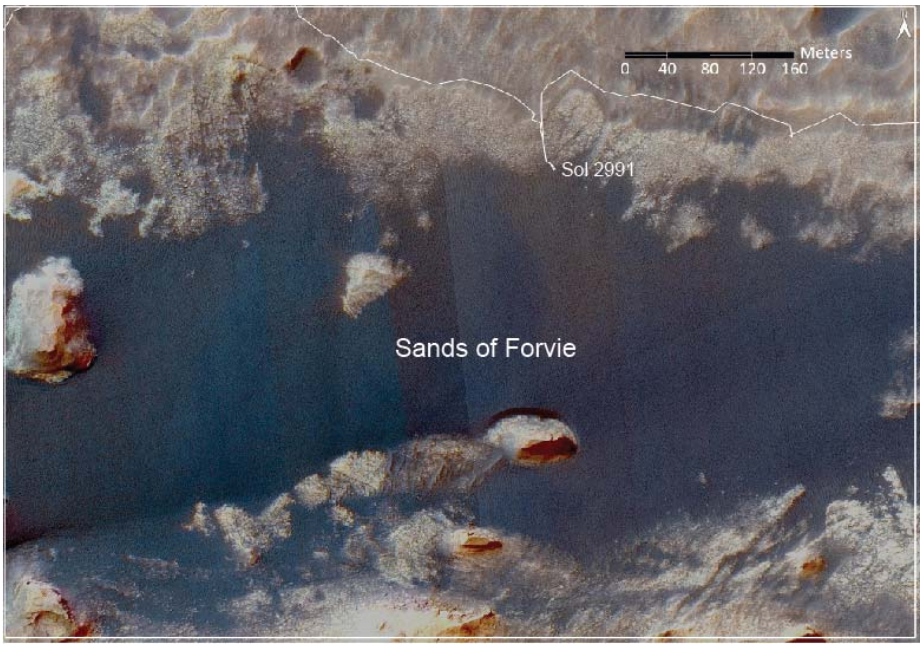

Figure 7. Portion of the HiRISE color mosaic centered on the Sands of Forvie sand sheet investigated by *Curiosity*. The location of the rover-based measurements is delineated by the sol 2991 location.

The deposit is covered with large transverse ripples that indicate a dominant wind direction moving toward the southwest (Sullivan et al., 2022; Figure 8).

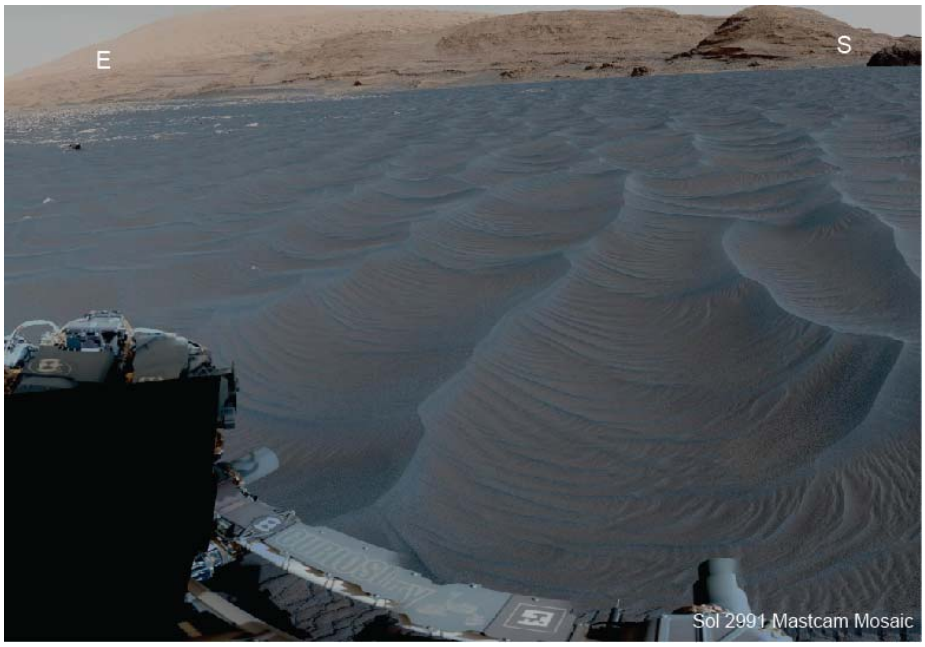

Figure 8. Portion of a Mastcam color mosaic taken on sol 2991 at the northern edge of the Sands of Forvie looking to the southeast into the sand sheet. Platy bedrock is evident in the mid-ground on the left side of the mosaic. Letters at the top of the figure denote direction. Image credit: NASA/JPL-Caltech/MSSS.

A subordinate direction is indicated by superimposed smaller ripples located in the larger ripple troughs (Figure 8). A *Curiosity*-based measurement campaign was conducted on the northern edge of the SoF sand deposit. Unfortunately, scoop samples were not acquired for delivery to CheMin. A left wheel scuff excavated across a transverse ripple crest and Mastcam color image data show that the surface exhibits a relatively reddish-brown color, whereas the interior contains darker sands intermixed with brighter grains (Figure 9). APXS data were acquired on four targets at the SoF measurement site: Braewick Beach, Airor, Ratharsair, and Traquir (Weitz et al., 2022). All four targets were compositionally similar, with low S, Cl, and Zn, consistent with low dust content expected on an active aeolian bedform. Grain sizes measured from MAHLI image data showed that the ripple crests contain slightly larger grains than the troughs, as is typical for the sand deposits studied by *Curiosity*, with evidence that the coarser grains correlate with high Ni content (Weitz et al., 2018, 2022).

Figure 9. Portion of a Mastcam color mosaic showing the scuff generated by the left front wheel in the Sands of Forvie. The sand is slightly cohesive and exhibits a reddish tint. Data acquired on Sol 2995 during *Curiosity*'s Sands of Forvie campaign. Note the presence of relatively bright grains in the scuffed sands, and the darker, bluer, coarser grains along this large ripple crest and flank. Image credit: NASA/JPL-Caltech/MSSS.

One of the considerations for *Curiosity*'s measurement campaigns for both sand deposits is that rover activities were accomplished at their margins. This was a consequence of the rover's mobility being highly limited in deep sands (Arvidson et al., 2016a). Given that the local bedrock adjacent to the sand deposits is relatively friable and produces a fine-grained regolith (e.g., Weitz et al., 2022), we investigated the extent of the contributions of sand grains weathered from local bedrock on the composition of the margin sand deposits. *Curiosity* acquired a pair of APXS measurements on the Fleurac sand targets located just to the north of the SoF. The APXS instrument fields of view (FOV) were offset by approximately two FOV radii (i.e., ~2 cm; VanBommel et al., 2016), with each containing a mixture of sand and blocky material disrupted from bedrock deposits (Figure 10).

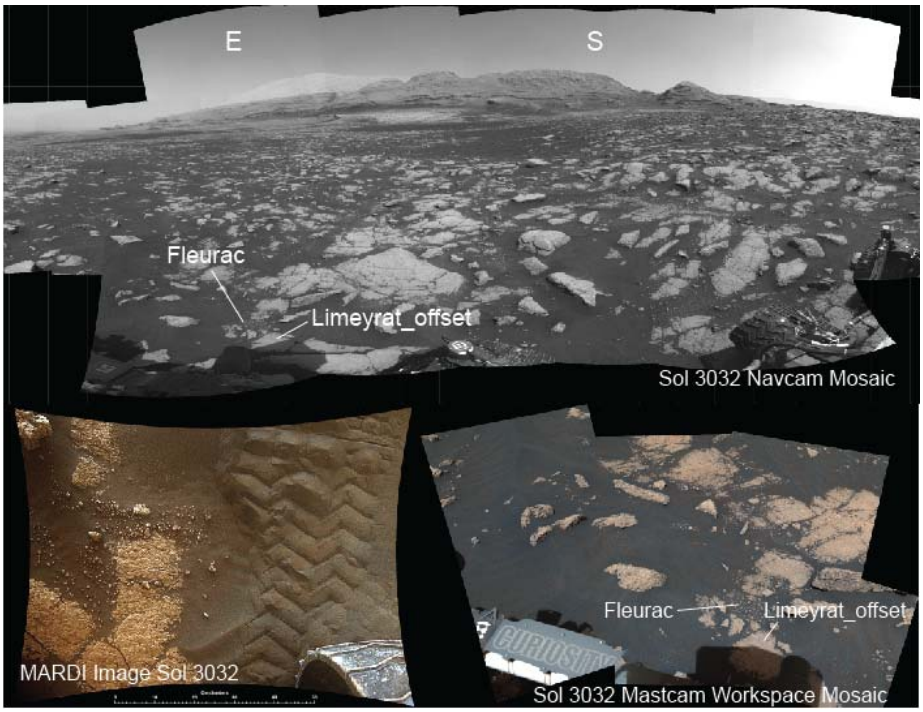

Figure 10. Portion of a Navcam mosaic taken on sol 3032 showing mixed boulders and sands located just to the north of the Sands of Forvie sand sheet. A MARDI image and Mastcam mosaic are also shown. The locations of the APXS Limeyrat_offset bedrock and the Fleurac observation is shown. Both the MARDI and Mastcam views show fragments of bedrock incorporated in relatively dark sands. Image credit: NASA/JPL-Caltech/MSSS.

The primary objective of paired measurements was to guard against APXS placement uncertainty (e.g., VanBommel et al., 2016) and to acquire a gradient in endmember (i.e., blocky material weathered from nearby bedrock and sand blown in from the main SoF sand sheet) coverage (Figures 10, 11).

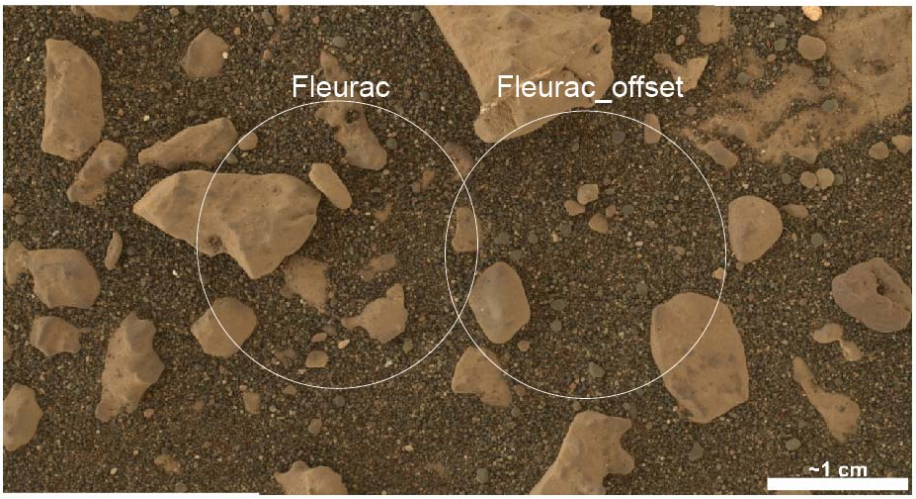

Figure 11. MAHLI color image of the two APXS Fleurac targets is shown. Circles represent the approximate fields of view of the APXS as deployed onto the surface. Fleurac contains a higher fraction of what appears to be cobble-size fragments of local bedrock whereas Fleurac_offset has a lower fraction. Both likely contain smaller local fragments mixed with sands from the Sands of Forvie. Image credit: NASA/JPL-Caltech/MSSS.

Deconvolution of the paired Fleurac measurements followed VanBommel et al. (2016, 2020), with deconvolution at the spectral level (e.g., VanBommel et al., 2019a, 2019b) as opposed to the derived oxides (e.g., VanBommel et al. 2016, 2017; Arvidson et al., 2016b; Stein et al., 2018). This approach provided superior accuracy in the final results; variability in sample relief was determined to be inconsequential (VanBommel et al., 2017). The spectral parameters within the deconvolution of the hypothesized wind-blown sand endmember were largely constrained due to numerous previous sand measurements where the contribution of locally disaggregated bedrock was assumed to be minimal (VanBommel et al., 2017). The presumed local regolith endmember was entirely unconstrained, aside from a closure requirement. The deconvolution analysis modeled the primary Fleurac target with 35% blocky material and 65% wind-blown sand, whereas the secondary offset target captured a combination of 10% blocky material and 90% wind-blown sand. These percentages are consistent with visual estimates from MAHLI images acquired with each APXS measurement location (Figure 11). The retrieved composition of the presumed locally derived regolith endmember most closely matched the composition of the nearby rock target Limeyrat_DRT, acquired one sol prior at the same investigation site (O'Connell-Cooper et al., 2022; Figure 10). A ratio plot of oxide compositions relative to a nearby sand composition shows that the calculational procedure was physically meaningful (Figure 12).

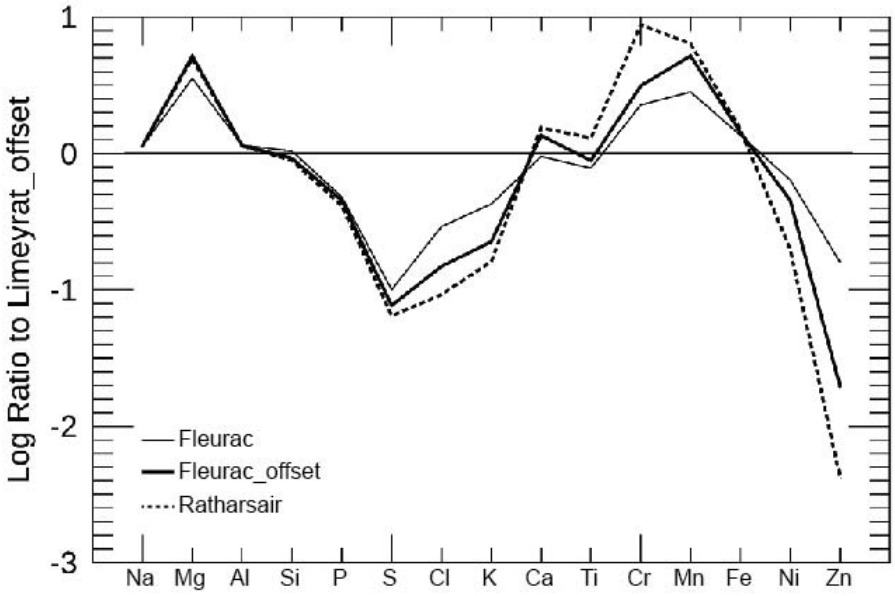

Figure 12. Natural log ratios of APXS data for the Fleurac experiment relative to the nearby rock target, Limeyrat_offset. The data for Fleurac are most like the rock target, followed by the Fleurac_offset, consistent with the visual appearance of rock fragment abundances shown in the MAHLI image (Figure 11). Ratharsair is an APXS target within a ripple trough the edge of the Sands of Forvie and is least like the rock target.

Specifically, the compositions change from more bedrock-like for the Fleurac measurement to less for the Fleurac_offset measurement, consistent with bedrock areal abundances as seen in the MAHLI image (Figure 11). Further, the trend toward more basaltic sand is consistent with the composition of the Ratharsair sand trough measurement obtained during the stop at the northern margin of SoF (see: Weitz et al., 2022).

To further illustrate the contributions of local bedrock, all APXS bedrock and sand measurements in the immediate vicinity of the MDI and SoF sampling locations were analyzed via correspondence analysis (CA) to evaluate relationships between compositional trends and target types (e.g., bedrock or sand). The analysis employed log ratio data to avoid known complications that can arise from normalized data sets (Aitchison, 1994) like APXS compositional data. The data used in the CA analysis for the MDI area were acquired between sols 1596 and 1677. For the SoF area the sol range was 2989-2994 and 3022-3047. We note that the sol 1606 Pogy measurement was not included because it is a compositional outlier, and initial analyses suggest the sample is a float rock. Two other measurements, Ash_Island (sol 1638) and Halftide_Ledge (sol 1647) were also excluded as compositional outliers. A CA bivariate plot of the first two most important eigenvector directions captures 84% of the variance in the APXS data

set, with locations of targets and oxides shown in Figure 13.

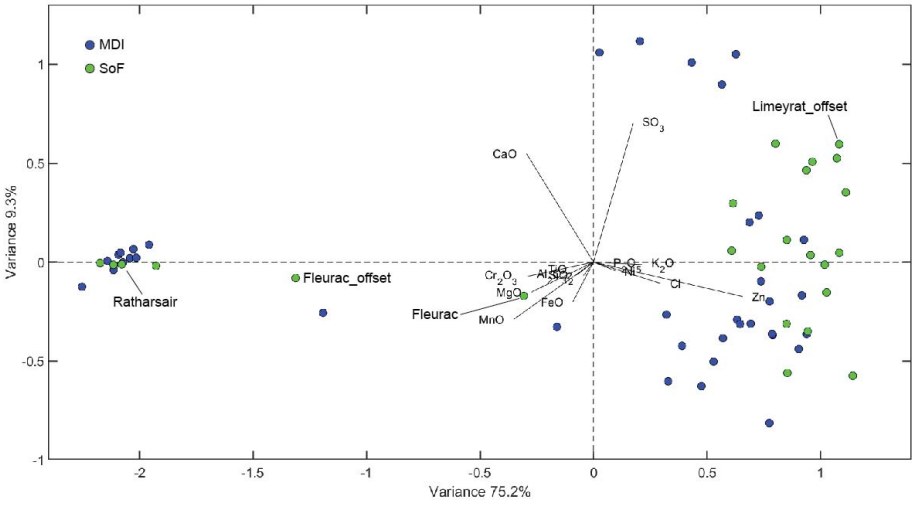

Figure 13. Correspondence analysis plot showing the relationship between APXS elemental abundances and targets for bedrock regions around Mount Desert Island and Sands of Forvie, together with measurements of the sand deposits at both sites. Note that the two sand deposit targets overlap, with Fleurac and Fleurac_offset located between the rock and sand targets. Also note the tight clustering of sand measurements for the two sites relative to the rock target data.

Bedrock data are clustered on one side of the plot, including the Limeyrat_offset target located near the Fleurac sand experiment site. The MDI and SoF sand measurements are clustered together on the left side of the plot. Fleurac and Fleurac_offset trend from the bedrock targets toward the sand targets, respectively. Note that Ratharsair, the SoF sand trough target, is also shown and falls within the sand cluster. Overall, the MDI and SoF sand targets are indistinguishable on the CA plot and in a direction consistent with the compositional dominance of ferrous silicate minerals. In summary, the Fleurac measurements and the overall compositional trends suggest that the APXS measurements at the margins of MDI and SoF are representative of their respective basaltic sand with minimal contributions from grains sourced from breakdown of local bedrock.

5 Mean CRISM Spectra for MDI and SoF Sand Deposits

Characteristics of Mean Spectra: The first step in examining spectral patterns for the MDI dunes and SoF sand sheet was to generate regions of interest (ROIs) for each deposit, with care not to include surrounding bedrock outcrops. The ROI boundary for the MDI dunes was limited to the northern extent of the CRISM ATO FRT00021C92. The ROIs, superimposed on the HiRISE mosaic, are shown in Figure 14 together with the mean spectra for the two areas. The spectral data extend from 0.50 to 2.6 µm, with the short wavelength cutoff

associated with increased noise at shorter wavelengths and the long wavelength cutoff chosen to avoid the rapid downturn associated with the presence of a deep ~3 µm absorption due to the presence of H_2O and M-OH, perhaps as adsorbed and/or absorbed molecules (e.g., He et al., 2022). Also shown on Figure 14 are the wavelengths used to generate the CRISM RGB false color images shown in Figures 1-3. The reddish-brown color of the Bagnold dunes, including the ROI, is associated with the upward slope of the MDI mean spectrum as opposed to the relatively flat longer wavelength trend for the SoF mean spectrum. Note that the SoF mean spectrum also has an overall lower SSA amplitude as compared to the MDI mean spectrum. This difference is intrinsic of the sands because the retrievals remove albedo variations associated with differences in lighting and viewing conditions.

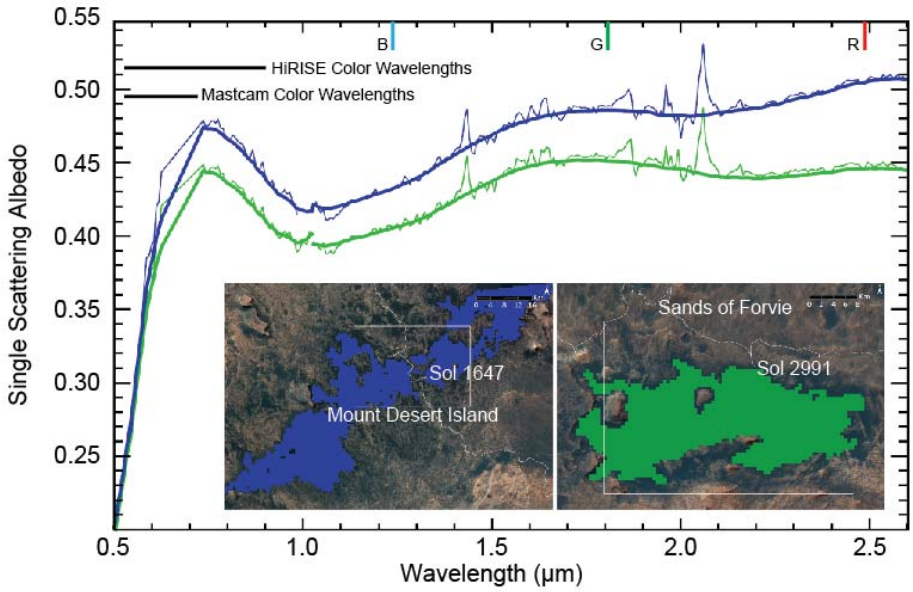

Figure 14. Mean spectral SSA plots from FRT00021C92 are shown for the regions of interest for the Mount Desert Island and Sands of Forvie. ROI coverages are shown overlain onto a portion of the HiRISE color mosaic. The Mount Desert Island ROI covers 3709 pixels whereas the Sands of Forvie ROI covers 1709 pixels at 12 m/pixel. Thick lines for the spectral plots were derived from the full log maximum likelihood processing of the data, whereas thin lines represent the means for the data before the processing. The wavelength regions between 0.62 and 0.72 µm are not included in analyses because they correspond to the instrument's blocking filter region. RGB labels correspond to the bands used to make the CRISM false color images displayed in Figures 1-3. Wavelength coverages for HiRISE and Mastcam color mosaics are also shown.

Both the MDI and SoF mean spectra converge for wavelengths shorter than ~0.75 µm result from the spectral dominance of ferric iron oxides and oxyhy-

droxides at shorter wavelengths (e.g., He et al., 2022). This is consistent with the observed reddish-brown colors in Mastcam images from both sites, given that both Mastcam and HiRISE color images are associated with these wavelengths, as shown on Figure 14. Johnson et al. (2004) show that thin coatings of iron oxides become less opaque at longer wavelengths over the spectral range shown in Figure 14. This phenomenon explains why the longer wavelength segments of the spectra are dominated by broad absorptions associated with ferrous silicate minerals. Thus, for detailed analyses of the mineralogy of MDI and SoF ROIs, we restrict the wavelength range to 0.9 to 2.5 µm where the data are controlled by the spectral properties of ferrous silicates within the deposits.

6 CRISM Spectral Endmembers Using Checkerboard Unmixing

The next step in analysis of MDI dune and SoF sand sheet spectra was to consider the spectral heterogeneity. There were two reasons for pursuing this topic. First was to understand the areal heterogeneity of the sand deposits for purposes of understanding the dynamics of deposition and transport. The second was to evaluate further contributions of local bedrock grains on the margins of the sand deposits, providing a much larger areal extent than obtained using APXS measurements. To pursue these objectives, we used a linear checkerboard unmixing approach with only L data (1.03 to 2.5 µm, 219 bands). This is because calculations with the combined S and L data showed that subtle pixel-to-pixel misregistration offsets at the joins of the two spectra strongly affected endmember selections. As explained in Section 2, the SMACC method takes the spectral data set and searches for endmembers that bound the hyperdimensional swarm. The program then treats each pixel and its respective spectrum as a linear combination of the endmember spectra.

The ROIs for the two sand deposits were run through the SMACC procedure as one data set under the simplifying assumption that the two deposits have the same mineral phases in different proportions to explain the differences for the long wavelength portions of the spectra. In fact, three endmembers explain 90% of the variance in the combined data set. The remaining 10% was found to be associated with aberrant spectra with unrealistic spectral shapes, presumably associated with ill-behaved portions of the 2D CRISM detector array (Murchie et al., 2007). Figure 15 shows the three endmember spectra, along with a color-coded relative abundance map. The endmember spectra include one (red trace) that is unlike the mean spectra shown in Figure 14, with a rise from 1.03 to 1.5 µm that curves to flat values at longer wavelengths. The abundance map indicates high proportions of this endmember at the margins of the two deposits and is interpreted to be a mixture of local bedrock and regolith incorporated into the basaltic sands, as shown in Figure 15. Examples of this local contamination can be seen as partially buried bedrock in Mastcam color images from MDI and SoF sand deposit locations (Figures 5 and 8).

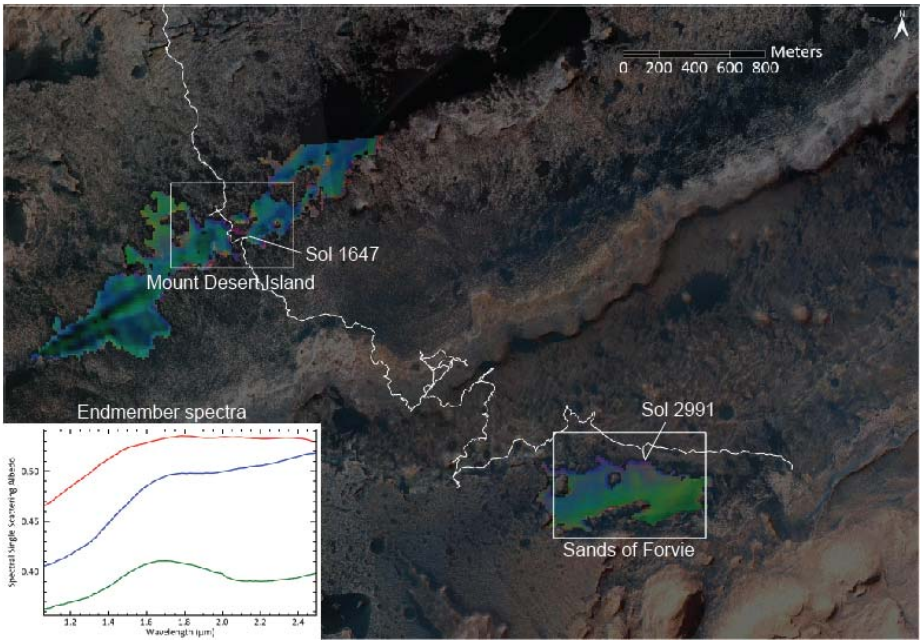

Figure 15. Results are shown for retrieval and concentration mapping of spectral endmembers for Mount Desert Island and Sands of Forvie. This assumes that the spectra mix linearly, i.e., in a checkerboard fashion. The three aerially important endmember spectra are shown on the lower left and mapped using the same color coding on the areas covered for the ROIs. The red spectrum and reddish colors mapped on the ROIs correspond to bedrock regions mapped within the intricate edges of the Mount Desert Island region and the southern part of the Sands of Forvie. The northern part of the Sands of Forvie maps as a mixture of bedrock contaminated areas and sand with an enhanced long wavelength positive slope (i.e., purple areas). The southern area within the sand sheet exhibits green colors typical of the mean for Sands of Forvie.

The other two endmember spectra share similarities with the mean spectra for the two sand deposits, one with a long wavelength rise (MDI, Figure 16) and the other with a broad and relatively deep ~2.2 µm absorption (SoF, Figure 17). Detailed analysis of the abundance map shows the former spectrum is more abundant in the MDI dune and the latter in the SoF sand sheet. The two spectra share a broad, not well defined, ~1 µm spectral feature that is also evident in the mean spectra for the two sand bodies. Note that endmember spectra shown in these latter two figures were derived by taking the means of the abundances for fractional proportions greater than 0.75 in each case.

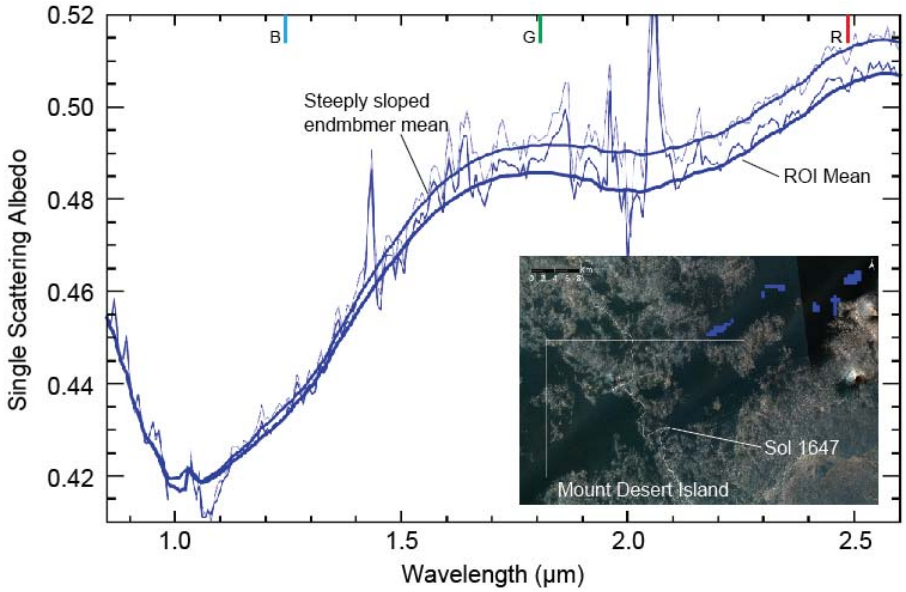

Figure 16. To delineate the region with the steepest spectral rise within the Mount Desert Island ROI, the highest valued areas with this endmember were retrieved using values >0.75 areal abundance/pixel. Both the means of the overall ROI and the highest concentration areas are plotted, with the highest concentration areas (fifty-two 12 m wide pixels) mapped as blue on the HiRISE color image.

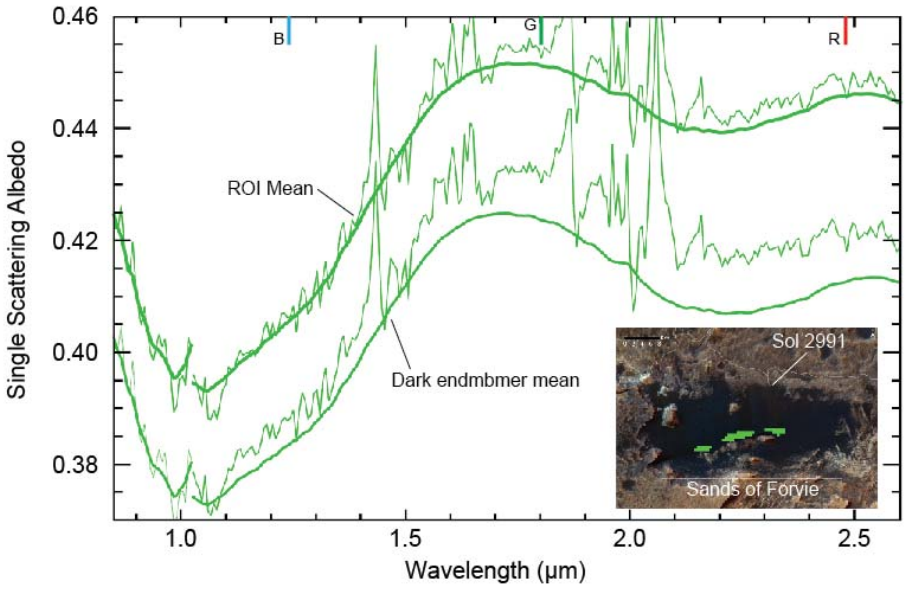

Figure 17. To delineate the region with the deepest ~2.2 µm absorption within the Sands of Forvie ROI the highest valued areas with this endmember were retrieved using values >0.75 areal abundance/pixel. Both the means of the overall ROI and the highest concentration areas are plotted, with the highest concentration areas (fifty-six 12 m wide pixels) mapped as green on the HiRISE color image.

The MDI endmember spectrum shows the dominance of the spectral pattern with an increasing value at longer wavelengths that is slightly brighter than the mean spectrum. On the other hand, the SoF spectral comparison shows that the spectral endmember is darker and has an even deeper ~2.2 µm absorption as compared to the mean value. In summary, the margins of the sand deposits do exhibit local bedrock contributions and the interior deposit endmembers do represent the extreme values that produce the spectral patterns evident in the mean spectra for the ROIs for the two deposits.

7 Hapke-based Retrieval of Mineral Abundances and Grain Sizes

Overview: The Hapke (2012) radiative transfer model was developed for particulate materials whose grain size is larger than the radiation wavelength and has a non-zero porosity. The MDI and SoF sand deposits are ideal candidates for use of this model, and it has been used previously with CRISM data for the Bagnold dunes complex to retrieve abundances and estimates of grain sizes for selected mineral phases (Kreisch et al., 2017; Lapotre et al., 2017a, 2017b; Rampe et al., 2018). As noted in Section 2, we employ an MCMC method developed by Lapotre (2017b) to retrieve relevant chemical and mineralogical information, after first retrieving optical constants from laboratory-based spectral reflectance data using methods based on Lucey (1998). These optical constants, along with grain size information, are needed by the MCMC unmixing algorithm to synthesize SSA spectra on the fly as it iterates over ranges of grain sizes that are input into the system. Based on grain size analyses of active aeolian sands in Weitz et al. (2018, 2022, and references therein), we allow a grain size range of 50-800 µm for each of our selected endmembers. We focus on modeling the endmember spectra for MDI and SoF deposits (Section 6) to ensure lack of contamination by local bedrock sources and to use spectra that have better diagnostic absorptions relative to the more mixed signals from the mean spectra. We also follow Occam's razor and use the minimum number of endmember spectra that explain the CRISM-based spectra for the MDI and SoF endmember spectra.

Selection of Endmember Spectra: As noted in Section 3, CheMin data for MDI sand samples show the presence, in order of decreasing amount, of an amorphous phase, plagioclase feldspar, olivine, pigeonite, and augite. We started computations with these phases, with an intent of using additional information to narrow down the range of compositions associated with these phases. We assume that, because of the lack of metal-OH combination bands and extensive H_2O combination bands in the spectral region of interest, the ubiquitous and relatively abundant XRD-amorphous phase within the sand deposits as found by CheMin (Rampe et al., 2018, 2020) is an igneous glass component, as op-

posed to amorphous products of, for example, aqueous alteration of primary material.

We proceeded initially by establishing a database of optical constants from reflectance data for candidate glasses and crystalline minerals typically found in sands dominated by basaltic compositions. Following the methods of Lucey (1998), we use the Hapke (2012) function along with assumed values of the real index of refraction and grain size diameters to invert and solve for the imaginary indices of refraction for each endmember. We use values for the real indices of refraction as given by Lapotre et al. (2017a), assuming that it remains constant over the wavelength range of 0.9 to 2.5 µm (Hiroi & Pieters, 1994). The average grain diameter represents the average of the sieved grain size ranges for each sample. We then proceeded to run many different combinations of models, retrieving mineral abundances and grain sizes for the MDI and SoF sand deposits. Consideration of the root mean square errors (RMSE) and correlation coefficients (R^2) between data and models allowed us to narrow down the range of likely components. As noted later in this section, a range of plausible results, rather than a single model, was a consequence of the nature of input spectral data and modeling methodology.

Amorphous Phase: Glasses with basaltic or near-basaltic compositions exhibit variable spectral reflectance patterns that are largely governed by the presence of iron. The broad spectral features centered near 1.05 µm and 1.9 µm in basaltic glasses are attributed to Fe^{2+} in octahedral and tetrahedral sites, respectively. (e.g., Bell et al., 1976; Cannon et al., 2017; Horgan et al., 2014). Additionally, coupling CheMin XRD mineralogy and APXS bulk chemistry gave different chemical compositions for amorphous components of Gobabeb and Ogunquit Beach sand samples (Rampe et al., 2020). To cover a range of possible Mars-like glass spectra resulting from different chemical compositions, we included a variety of endmember spectra from synthetic glass samples generated using APXS-based compositional measurements (e.g., McSween et al., 2008, normalized to SO_3 = Cl = 0.0 wt.%) acquired by the Spirit rover for representative rocks and basaltic soils (rocks Wishstone, Irvine, Clovis, Grahamland, Gusev Mean Soil, Panda, Doubloon, and Independence; Table S1). The Spirit-based measurements are relevant because numerous measurements were made by this rover, thereby providing a range of samples and associated reflectance spectra and chemical compositions. Refer to Supporting Information for chemical compositions and synthesis procedures. For completeness, we also included a terrestrial glass sample from Hawaii (C1BE100_Gl) whose spectrum was employed in previous spectral-modeling studies as the amorphous component (Lapotre et al., 2017a; Rampe et al., 2018).

Plagioclase: CheMin data for the Ogunquit Beach MDI dune sample showed a composition of $An_{48\pm5}$ (i.e., labradorite) for the feldspar component (Rampe et al., 2018). Earlier CheMin sand analyses have calculated additional plagioclase compositions of $An_{49\pm4}$ and $An_{63\pm5}$ (Rampe et al., 2020). The labradorite sample selected for our modeling provides a representative spectrum of plagio-

clase, with a shallow and broad ~1.2 µm feature due to iron in the crystal structure (Burns, 1970; Crown et al., 1987). This feature tends to be ubiquitous in basaltic assemblages (Adams et al., 1978; Crown et al., 1987), and the labradorite spectrum was considered by us to be a suitable endmember spectrum for our calculations.

Olivine: In olivine, Fe^{2+} and Mg^{2+} partition between the smaller M1 and larger M2 sites based on multiple factors including ion size configuration of the crystallographic site (Burns, 1970; Dyar et al., 2009). Olivine exhibits three absorption bands due to spin allowed Fe^{2+} transitions in Fe^{2+} residing in both the M1 and M2 cation sites (Burns, 1970, 1993; Sunshine et al., 1998; Trang et al., 2013). The two M1 site absorptions are centered at ~0.85 and 1.25 µm, whereas the single M2 band is centered at ~1.03-1.05 µm. These features overlap to form a broad absorption envelope centered near 1 µm (Burns, 1970).

The olivine composition determined by CheMin for the sand deposits (Rocknest, Gobabeb, and Ogunquit Beach) have a mean composition of $Fo_{55\pm5}$ (Achilles et al., 2017). We utilized a spectrum for our modeling that was acquired for a Fo_{51} sample (Table 2). This sample was chosen because the composition is within the range found in-situ by CheMin, has a well-defined broad 1 µm Fe^{2+} olivine spectral feature, minimal extraneous spectral features (i.e., from chromium or titanium), and a well-documented chemistry (Kokaly et al., 2017).

Pyroxenes: Clinopyroxenes, primarily pigeonite and augite, have been detected as a significant component of sand deposits in Gale crater (Achilles et al., 2017; Ehlmann et al., 2017; Rampe et al., 2018). CheMin-based pyroxene analyses do not readily distinguish among pyroxene minerals, because instrumental limitations result in strong overlap of the pyroxene diffraction peaks (Achilles et al., 2017; Rampe et al., 2018). Thus, pyroxene spectra were chosen based on compositions of Martian meteorites Elephant Moraine EET 79001 for pigeonite ($Wo_{10\text{-}11}En_{61\text{-}45}Fs_{29\text{-}44}$; McFadden et al., 2005) and Lafayette for augite ($Wo_{37\text{-}40}En_{35\text{-}41}Fs_{20\text{-}28}$; Boctor et al., 1976). However, reflectance spectra for bulk meteorite samples represent a mixture of minerals (felspar as diaplectic glass) rather than pure pyroxene signatures. Thus, we chose spectra for pure, synthetic pyroxene samples that have comparable compositions to the pyroxenes in Martian meteorites as stated above (Tables 1, 2).

Relationship to previous studies: Our spectral endmember set is similar to that utilized by Lapotre et al. (2017a) and Rampe et al. (2018) in their SSA-based analyses of sands from the Bagnold dunes. Both sets used plagioclase (labradorite), Fo_{51} olivine, pigeonite, and augite, with basaltic glass as the amorphous component. The significant difference is in the chemical composition of the glass component. We use a variety of potential basaltic glass endmembers having a range of Mars-like chemical compositions derived from chemical compositions of Martian basalts at Gusev crater. The above authors used a basaltic glass from Hawaii (C1BE100) and additionally incorporated a magnetite endmember. As discussed next, the glass is a significant spectral component, so that chemical compositions derived by inverting spectral data depend on the

chemical composition of the glass whose spectral properties complement the best fit the model. More simply, two glasses with equivalent spectral properties but different chemical compositions necessarily result in two valid sets of derived chemical compositions.

Model Results: For each glass endmember, we ran 2000 unmixing models using MCMC while always including plagioclase, olivine, and pyroxene as part of the assemblage (Table S2). As noted by Lapotre et al. (2017a) spectral unmixing is nonunique, where tradeoffs between grain sizes and abundances can produce similar spectral features. The advantage of MCMC is that it solves for the probability density functions of each endmember's abundance and grain size (i.e., it provides a range of possible solutions). To that end, we used violin plots to show the probability density functions superimposed on box-and-whisker plots to provide a visual representation of the distribution of the data, along with basic measures of central tendency (Hintze & Nelson, 1998). Some glass endmembers produced only a small number (~a dozen) good fits and were eliminated from consideration. The GMS_Gl (Gusev Mean Soil), Grahamland_Gl, and C1BE100_Gl endmembers produced the largest number (30) of best fit models (RMSE 0.005 and R^2 0.96) for both sand deposits. These runs also produced similar trends in mineral abundances and grain sizes.

As an illustrative example of model runs, we show in Figure 18 the SSA endmember spectra and model results that had the lowest RMSE and highest R^2 between the data and retrieved models using GMS_Gl for the glass endmember.

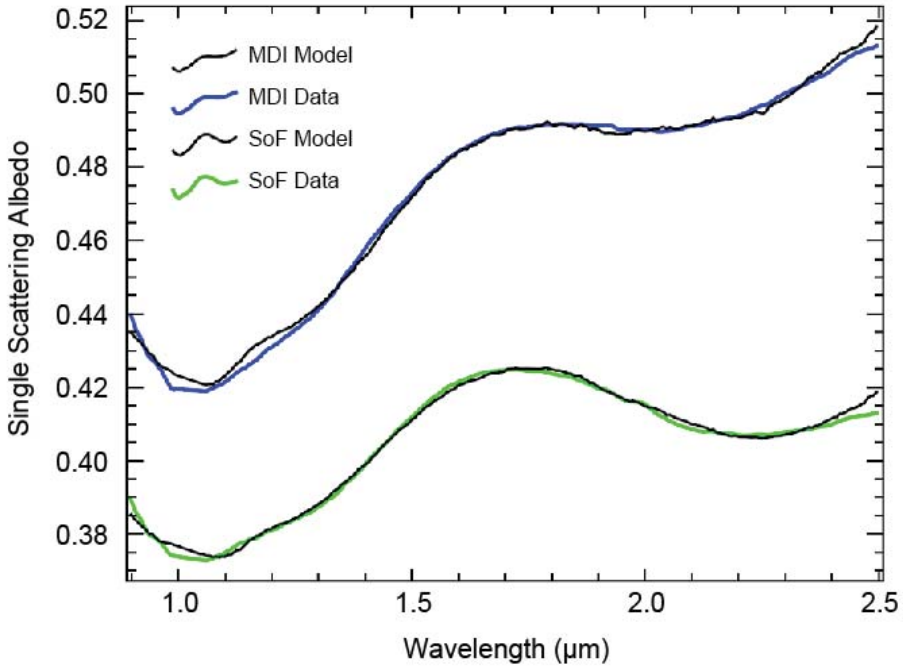

Figure 18. Plots are shown for the lowest RMSE differences between the endmember spectra for Mount Desert Island and Sands of Forvie and Hapke nonlinear modeling. The wavelength interval centered on 1.00 to 1.08 µm is blanked out because of increased uncertainty of retrieved spectra because of low sensitivity at the wavelength limits for the S and L spectrometers.

Specifically, the MDI sand endmember best fit had an RMSE of 0.00165 and an R^2 of 0.997, and the SoF sand endmember best fit had an RMSE of 0.00124 and an R^2 of 0.994. Figures 19 and 20 also show these spectra, along with the simulated SSA spectra that the procedure chose as the best fit combination to make the model spectrum. The retrieved mineral abundances and grain sizes are also shown. For both deposits, GMS glass and labradorite are the most abundant phases, similar to the rankings of the amorphous phase(s) and feldspar abundances as determined by CheMin for the MDI sand sample (Rampe et al., 2020). GMS glass and labradorite, in addition to any olivine present in both deposits, contribute to the broad 1 µm feature observed in both MDI and SoF spectra (Figures 16 and 17). Between MDI and SoF, the main spectral difference (other than albedo) is in the relative proportions of the two pyroxenes (pigeonite and augite). The long wavelength spectra rise for MDI is consistent with the model result pigeonite/augite = 4.8, and the SoF ~2.2 µm spectral minimum is consistent with the model result pigeonite/augite = 0.0 (Figures 19 and 20). Grain size results, which in the Hapke (2012) model are much less constrained relative to phase abundances (Lapotre et al., 2017a), show a slight trend of coarser grains for SoF as compared to MDI deposits. This result is consistent with MAHLI-based observations from Curiosity (Weitz et al., 2022).

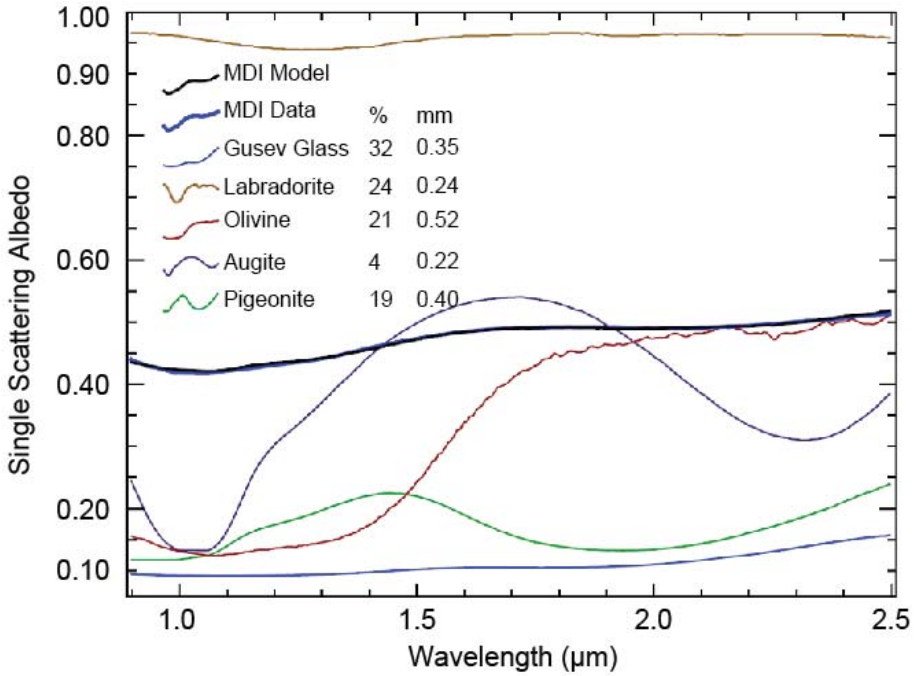

Figure 19. Plot showing the same data and lowest RMSE model fit for Mound Desert Island as shown in Figure 18, together with the SSA spectra for end-members used to model the data. The weight abundances and grain sizes are provided in the caption on the plot.

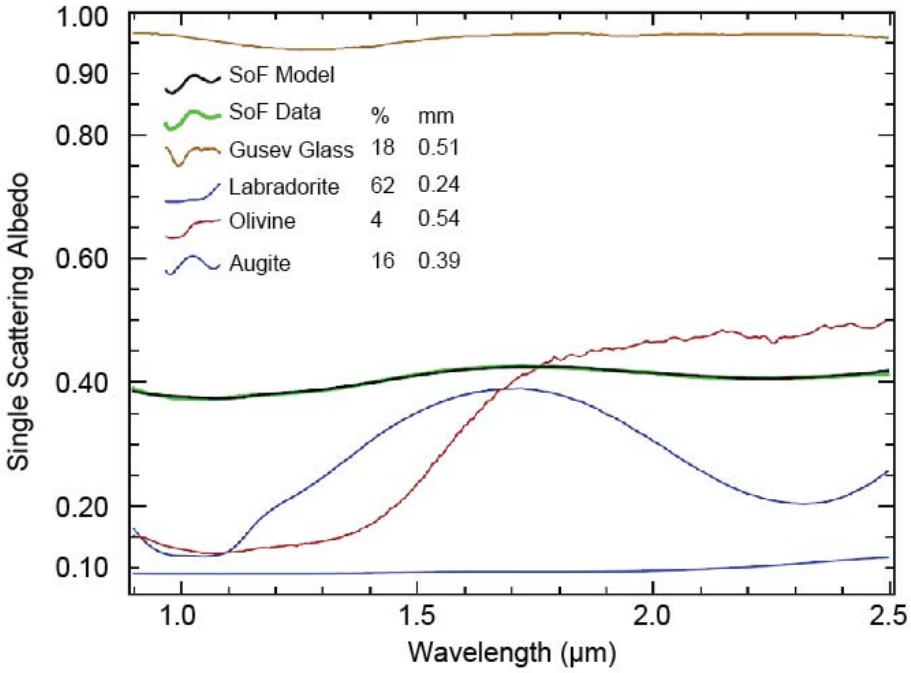

Figure 20. Plot showing the same data and lowest RMSE model fit for Sands of Forvie as shown in Figure 18, together with the SSA spectra for endmembers used to model the data. The weight abundances and grain sizes are provided in the caption on the plot.

Violin plots for model runs discussed above are shown in Figure 21 for the two endmember spectra. Only model runs with RMSE 0.005 and R^2 0.96 are included in the violin plots, which amounts to 83 model runs using the MDI deposit endmember spectrum and 46 model results using the SoF deposit endmember spectrum. These plots show a wide range of results, as expected from the nonunique nature of the model. We do note that the trends in the data follow what we described for the two best fits. This leads us to conclude that the GMS glass and labradorite are the most abundant phases and primarily responsible for controlling the overall albedo of the MDI and SoF spectral endmembers. Spectral differences at longer wavelengths are likely controlled by the relative proportions of the two pyroxenes in each deposit. Further, the grain sizes are generally larger for the SoF as opposed to the MDI deposits.

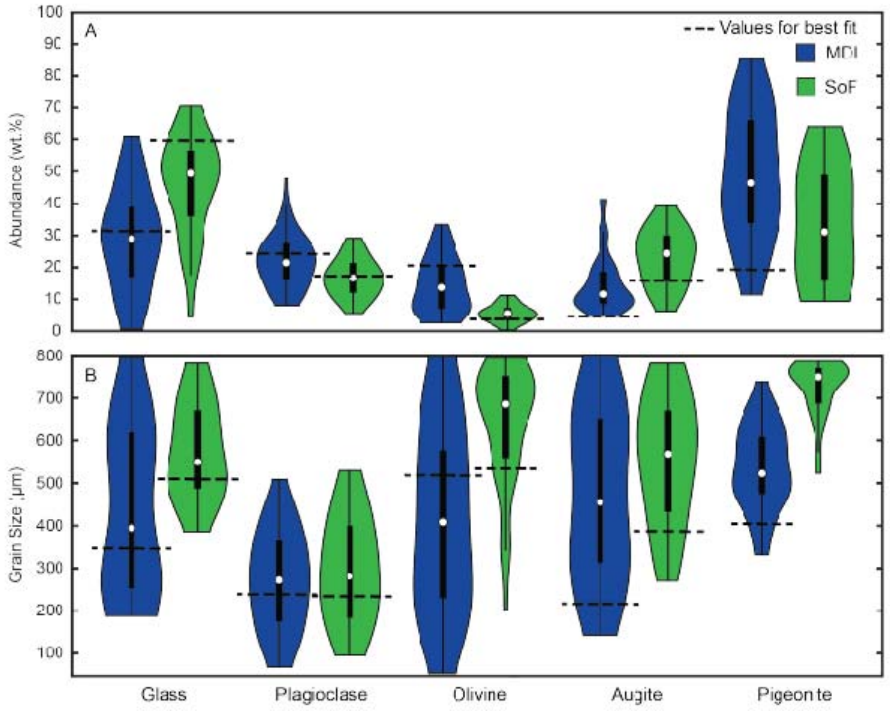

Figure 21. Probability density violin plots (Hintze & Nelson, 1998) for model runs. Violin plots show distribution of (a) weight abundances (wt.%) and (b) grain sizes (µm) for each endmember. Horizontal dashed lines show the values for the lowest RMSE fits for the two sand bodies.

Inversions of Spectra to Chemical Compositions: Following the approach outlined by Lapotre et al. (2017b), we inverted the mineral-based results for our two endmember results to examine compositional trends, simulating compositions that would have been obtained by APXS (Table S3). Specifically, following VanBommel et al. (2019a, 2019b), we did the inversions by first starting with APXS spectra instead of oxides. This approach mitigates matrix effects within XRF (e.g., APXS) data that can result in inaccuracies when performing similar analyses via oxide mass balance. The simulated APXS spectra were then converted to oxide abundances.

Following Lapotre et al. (2017a), we plot model results on a SiO_2 vs. MgO+FeO diagrams for all our CRISM spectral retrieval results, along with compositions for the endmember spectra used in the CRISM-based retrievals (Figure 22). Results highlight the similarities between the two sand sheets in terms of the cluster of results located in the approximately the same values of SiO_2 vs. MgO+FeO. Results also show the dominance of pigeonite in controlling the differences between the two sand bodies. Finally, it is noted that the best fit model results are not centered with the bulk of the model results, again demonstrating that

the models need to be examined in a strict statistical sense.

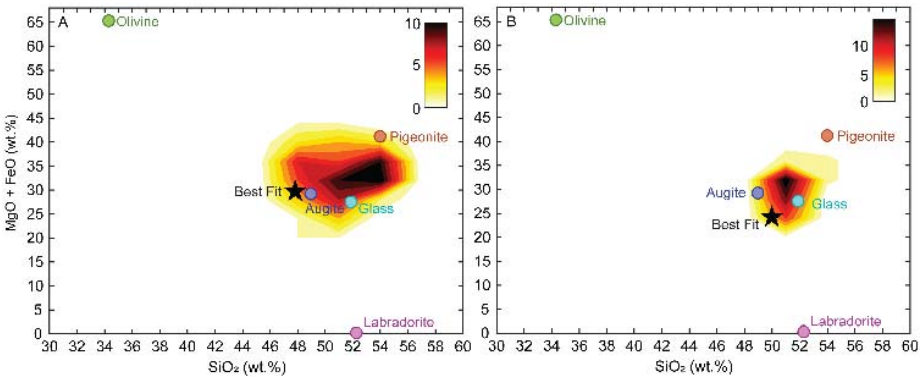

Figure 22. Calculated SiO_2 vs. MgO + FeO for all accepted model runs for (a) MDI and (b) SoF, displayed as heatmaps. Dark red color indicates a higher concentration of points, while white means there are no points in that space. Mineral endmembers are displayed as colored circles, while the best fit model run for each MDI and SOF is a star.

8 Conclusions and Implications

Multiple CRISM false-color image data show that the linear Bagnold dunes in Gale Crater have a reddish-brown color, while sand sheets to the south of the dunes are darker and lack the reddish-brown color. The traverse of the *Curiosity* rover has led to observations of the linear dunes at Mt. Desert Island (MDI), and a sand sheet to the south at the Sands of Forvie (SoF). SSA spectra retrieved from CRISM scene FRT00021C92 show that the difference in the false-color images can be attributed to a long wavelength (1.7 to 2.5 µm) rise in the MDI sand spectrum that is absent in the SoF spectrum. Instead, the SoF sand spectrum is characterized by a broad ~2.2 µm absorption feature.

To classify the potential mineralogic controls on these different spectral features, we performed checkerboard unmixing of the SSA image cube to extract the extreme spectral endmembers from both sand deposits. These spectra were modeled using carefully selected laboratory spectra and Hapke (2012) theory to invert for mineral abundances and grain size information. Model results, including inversions to equivalent APXS oxide compositions, show that spectral endmembers from both sites are dominated by basaltic glass (i.e., an amorphous phase) and labradorite or other spectrally equivalent feldspar. The broad 1 µm feature in both MDI and SoF is primarily controlled by olivine, with some contribution from basaltic glass. Inclusion of a pigeonite spectrum explains the increase in SSAs with increasing wavelength for the MDI spectral endmember, while the absence of pigeonite and presence of augite explains the deep, broad ~2.2 µm absorption for the SoF spectral endmember. Modeling results also suggest that the SoF deposit has coarser grains than the MDI deposit, consistent with measurements from MAHLI data (Weitz et al., 2022). Importantly,

modeling reflectance data displayed the non-uniqueness of deriving chemical composition from CRISM data and highlighted the importance of statistical analysis of the data.

The primary emphasis of the paper was to retrieve the mineralogy and grain sizes for MDI and SoF and to compare to observations acquired by Curiosity, but there are also implications for aeolian processes. First, we note that the two sand bodies are only ~2.5 kilometers from one another. Even given their proximity, they have subtle yet distinctly different mineralogy and grain sizes. We speculate that the differences are a consequence of the topographic settings intensifying wind sorting effects over time. The Bagnold linear dunes are not encumbered by topography, but rather are migrating from NE to SW associated with the dominate wind direction (Sullivan et al., 2022). On the other hand, the SoF is bordered on the south and southwest by topographic obstacles, specifically the hills associated with Mount Sharp and the scarp that defines the edge of the Greenheugh pediment (Figure 23). The sands in SoF are thus unable to migrate in an unencumbered manner. We infer that the finest grained sands preferentially migrate onto the pediment surface, leaving behind overall coarser material and a slightly different mineralogy as compared to the Bagnold dune sands. The remaining grains left behind can become segregated by wind conditions saltating smaller grains but causing creep of larger grains. This can lead to coarsening of the ripples, ultimately causing the formation of coarse-grained megaripples as observed in SoF (Lapotre et al., 2018). This cycle causes the variation seen in the spectral data, that is, SoF contains larger ripples with concentrated coarser grains while MDI lacks this coarsening and has smaller ripples.

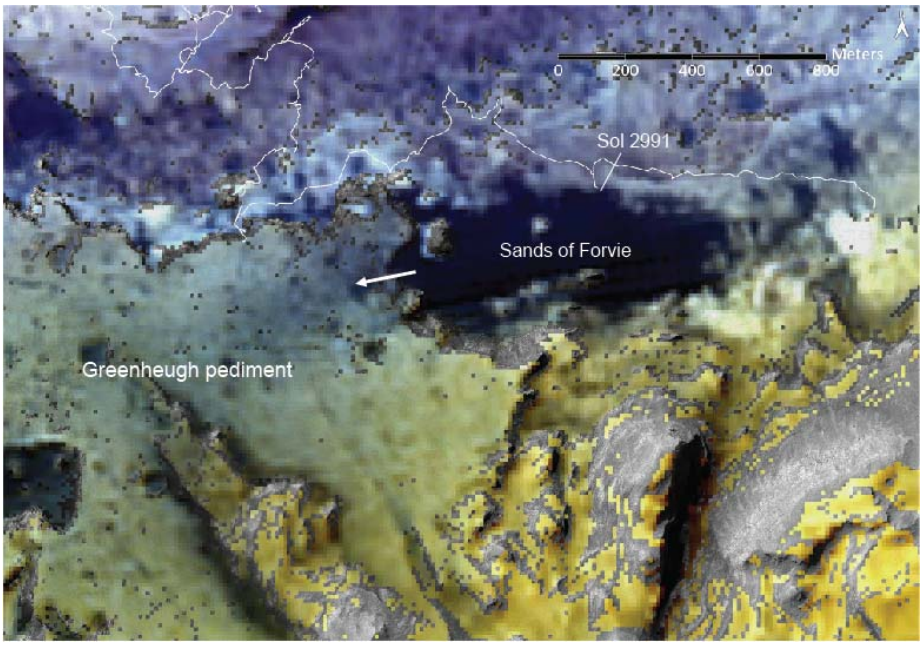

Figure 23. FRT00021C92-based false color image with 50% transparency over red version of the HiRISE mosaic. The figure covers the SoF and eastern side of the Greenheugh pediment. Arrow represents inferred wind direction for sands derived from SoF and deposited on the pediment, together with local bedrock-derived sediment also blown onto the pediment. RGB set to 0.618, 0.553, 0.468 µm. Slopes >15° were excised from the FRT image to enhance the color variations associated with relatively flat terrain.

Second, there is a potential that these two deposits have different source materials. In our study, olivine is the heaviest mineral with augite and pigeonite having approximately equal densities. Topographic influence and wind sorting alone may not be enough to explain the variation in pyroxene abundances observed through spectral modeling results, as wind sorting would not separate the pyroxene minerals. The combination of unique source material and topographic influence, however, could then explain the outcomes of this study observed from spectral data. In this case, SoF would have been sourced from a more augite-rich material compared to MDI.

Finally, our result has implications for interpreting aeolian deposits in the Martian rock records. Here we have two sand bodies that are close to one another yet have different properties. This is an example of the paradigm that "present is the key to the past". The aeolian rock record likely has similar examples of deposits in the same stratigraphic horizon, but with laterally varying properties controlled by local topographic or other controls. Unique properties observed within aeolian rocks could provide insights into more regional variations of topography, wind regime, and mineral sorting.

9 Acknowledgments

The work presented in this paper was partially supported by Contract 1549716 from the Caltech/Jet Propulsion Laboratory to REA, MNH, and SJV, for participation on the Mars Science Laboratory *Curiosity* rover mission. RVM acknowledges support from the NASA Mars Science Laboratory *Curiosity* rover mission and the NASA Johnson Space Center. We thank Loan Le (Jacobs, Johnson Space Center) for synthesis and electron microprobe analyses of synthetic glasses.

10 Data Availability Statement

The data sets used in this study are publicly available through the Planetary Data System Geosciences Node (https://pds-geosciences.wustl.edu/). The HiRISE data are available at https://www.uahirise.org/. CRISM, Navcam, Mastcam, MARDI, MAHLI, and APXS raw data can be found at https://pds-geosciences.wustl.edu/dataserv/doi.htm. Mastcam, MAHLI, and MARDI mosaics were processed by the Mastcam team at Malin Space Science Systems (MSSS). Laboratory mineral spectra are available through the PDS/RELAB (https://pds-speclib.rsl.wustl.edu/) and the USGS (https://www.usgs.gov/labs/spectroscopy-lab/science/spectral-library) spectral libraries, while the synthetic glass spectra can be found at https://openscholarship.wustl.edu/data/102/. The product IDs and DOIs of all data sets used in this study are also listed in Table 1.

11 References Cited

Achilles, C.N., Downs, R.T., Ming, D.W., Rampe, E.B., Morris, R.V., Treiman, A.H., et al. (2017). Mineralogy of an active eolian sediment from the Namib dune, Gale crater, Mars. *Journal of Geophysical Research: Planets*, *122*(11), 2344–2361. https://doi.org/10.1002/2017JE005262

Adams, J.B., & Goullaud, L.H. (1978). Plagioclase feldspars: visible and near infrared diffuse reflectance spectra as applied to remote sensing. *Proceedings of the Lunar Science Conference*, *9*, 2901–2909.

Aitchison, J. (1994). Principles of compositional data analysis. *Lecture Notes-Monograph Series*, *24*, 73–81. https://doi.org/10.1214/lnms/1215463786

Arvidson, R.E., Iagnemma, K.D., Maimone, M., Fraeman, A.A., Zhou, F., Heverly, M.C., et al. (2016a). Mars Science Laboratory Curiosity Rover Megaripple Crossings up to Sol 710 in Gale Crater. *Journal of Field Robotics*, *34*(3), 495–518. https://doi.org/10.1002/rob.21647

Arvidson, R.E., Poulet, F., Morris, R.V., Bibring, J.P., Bell, J.F. III, Squyres, S.W., et al. (2006). Nature and origin of the hematite-bearing plains of Terra Meridiani based on analyses of orbital and Mars Exploration rover data sets. *Journal of Geophysical Research E: Planets*, *111*(12), 1–19. https://doi.org/10.1029/2006JE002728

Arvidson, R.E., Squyres, S.W., Morris, R.V., Knoll, A.H., Gellert, R., Clark, B.C., et al. (2016b). High concentrations of manganese and sulfur in deposits on Murray Ridge, Endeavour Crater, Mars. *American Mineralogist*, *101*(6), 1389–1405. https://doi.org/10.2138/am-2016-5599

Bell III, J.F., Godber, A., McNair, S., Caplinger, M.A., Maki, J.N., Lemmon, M.T., et al. (2017). The Mars Science Laboratory Curiosity rover Mastcam instruments: Preflight and in-flight calibration, validation, and data archiving. *Earth and Space Science*, *4*(7), 396–452. https://doi.org/10.1002/2016EA000219

Bell III, J.F., Malin, M.C., Caplinger, M.A., Ravine, M.A., Godber, A.S., Jungers, M.C., et al. (2012). Mastcam Multispectral Imaging on the Mars Science Laboratory Rover: Wavelength coverage and imaging strategies at the Gale Crater field site. *43rd Lunar and Planetary Science Conference*, No. 2541.

Bell, P.M., Mao, H.K., & Weeks, R.A. (1976). Optical spectra and electron paramagnetic resonance of lunar and synthetic glasses: A study of the effects of controlled atmosphere, composition, and temperature. *Proceedings of the Lunar Science Conference*, *7*, 2543–2559.

Bennett, K., et al. (2022). An Overview of Curiosity's Campaign in Glen Torridon and Synthesis of Major Results, *Journal of Geophysical Research: Planets*, submitted.

Bennett, K.A., Hill, J.R., Murray, K.C., Edwards, C.S., Bell, J.F. III, & Christensen, P.R. (2018). THEMIS-VIS Investigations of Sand at Gale Crater. *Earth and Space Science*, *5*(8), 352–363. https://doi.org/10.1029/2018EA000380

Blake, D., Vaniman, D., Achilles, C., Anderson, R., Bish, D., Bristow, T., et al. (2012). Characterization and calibration of the CheMin mineralogical instrument on Mars Science Laboratory. *Space Science Reviews*, *170*(1–4), 341–399. https://doi.org/10.1007/s11214-012-9905-1

Boctor, N.Z., Meyer, H.O.A., & Kullerud, G. (1976). Lafayette Meteorite: Petrology and Opaque Mineralogy. *Earth and Planetary Science Letters*, *32*, 69–76. https://doi.org/10.1007/s12036-014-9301-1

Bridges, N.T., & Ehlmann, B.L. (2018). The Mars Science Laboratory (MSL) Bagnold Dunes Campaign, Phase I: Overview and introduction to the special issue. *Journal of Geophysical Research: Planets*, *123*(1), 3–19. https://doi.org/10.1002/2017JE005401

Burns, R.G. (1970). Crystal Field Spectra and Evidence of Cation Ordering in Olivine Minerals. *American Mineralogist*, *55*(9-10), 1608–1632.

Burns, R.G. (1993). Origin of electronic spectra of minerals in the visible and near-infrared region. In C. M. Pieters & P. A. Englert (Eds.), *Remote Geochemical Analysis* (pp. 3–29).

Calef III, F.J., & Parker, T. (2016). MSL Gale Merged Orthophoto Mosaic [Data Set]. PDS Annex, U.S. Geological Survey. http://bit.ly/MSL_Basemap

Cannon, K.M., Mustard, J.F., Parman, S.W., Sklute, E.C., Dyar, M.D., & Cooper, R.F. (2017). Spectral properties of Martian and other planetary glasses and their detection in remotely sensed data. *Journal of Geophysical Research: Planets*, *122*(1), 249–268. https://doi.org/10.1002/2016JE005219

Christian, J.R., Arvidson, R.E., O'Sullivan, J.A., Vasavada, A.R., & Weitz, C.M. (2022). CRISM-based High Spatial Resolution Thermal Inertia Mapping along Curiosity's Traverses in Gale Crater. *Journal of Geophysical Research: Planets*. https://doi.org/10.1029/2021je007076

Crown, D.A., & Pieters, C.M. (1987). Spectral properties of plagioclase and pyroxene mixtures and the interpretation of lunar soil spectra. *Icarus*, *72*(3), 492–506. https://doi.org/10.1016/0019-1035(87)90047-9

Dyar, M.D., Sklute, E.C., Menzies, O.N., Bland, P.A., Lindsley, D., Glotch, T., et al. (2009). Spectroscopic characteristics of synthetic olivine: An integrated multi-wavelength and multi-technique approach. *American Mineralogist*, *94*(7), 883–898. https://doi.org/10.2138/am.2009.3115

Edgett, K.S. (2013). MSL Mars Hand Lens Imager 4 RDR ZSTACK V1.0 [Data set]. NASA Planetary Data System. https://doi.org/https://doi.org/10.17189/1520169

Edgett, K.S., Yingst, R.A., Ravine, M.A., Caplinger, M.A., Maki, J.N., Ghaemi, F.T., et al. (2012). Curiosity's Mars Hand Lens Imager (MAHLI) investigation. *Space Science Reviews*, *170*(1–4), 259–317. https://doi.org/10.1007/s11214-012-9910-4

Edwards, C.S., Piqueux, S., Hamilton, V.E., Fergason, R.L., Herkenhoff, K.E., Vasavada, A., et al. (2018). The Thermophysical Properties of the Bagnold Dunes, Mars: Ground-Truthing Orbital Data. *Journal of Geophysical Research: Planets*, *123*(5), 1307–1326. https://doi.org/10.1029/2017JE005501

Ehlmann, B.L., Edgett, K.S., Sutter, B., Achilles, C.N., Litvak, M.L., Lapotre, M.G.A., et al. (2017). Chemistry, mineralogy, and grain properties at Namib and High dunes, Bagnold dune field, Gale crater, Mars: A synthesis of Curiosity rover observations. *Journal of Geophysical Research: Planets*, *122*(12), 2510–2543. https://doi.org/10.1002/2017JE005267

Gellert, R. (2013). MSL Mars Alpha Particle X-Ray Spectrometer 4/5 RDR V1.0 [Data Set]. NASA Planetary Data System. https://doi.org/10.17189/1518757

Gellert, R., Clark III, B.C. (2015). In Situ Compositional Measurements of Rocks and Soils with the Alpha Particle X-ray Spectrometer on NASA's Mars Rovers. *Elements*, *11*(1), 39–44. https://doi.org/10.2113/gselements.11.1.39

Grotzinger, J.P., Gupta, S., Malin, M.C., Rubin, D.M., Schieber, J., Siebach, K., et al. (2015). Deposition, exhumation, and paleoclimate of an ancient lake deposit, Gale crater, Mars. *Science*, *350*(6257).

https://doi.org/10.1126/science.aac7575

Grotzinger, J.P., Crisp, J., Vasavada, A.R., Anderson, R.C., Baker, C.J., Barry, R., et al. (2012). Mars Science Laboratory mission and science investigation. *Space Science Reviews*, *170*, 5–56. https://doi.org/10.1007/s11214-012-9892-2

Gruninger, J.H., Ratkowski, A.J., & Hoke, M.L. (2004). The sequential maximum angle convex cone (SMACC) endmember model. *Algorithms and Technologies for Multispectral, Hyperspectral, and Ultraspectral Imagery X*, *5425*. https://doi.org/10.1117/12.543794

Hapke, B. (2012). *Theory of Reflectance and Emittance Spectroscopy* (2nd ed.). Cambridge, UK: Cambridge University Press. https://doi.org/10.1017/CBO9781139025683

He, L., Arvidson, R.E., O'Sullivan, J.A., Morris, R.V., Condus, T., Hughes, M.N., & Powell, K.E. (2022). Surface Kinetic Temperatures and Nontronite Single Scattering Albedo Spectra from Mars Reconnaissance Orbiter CRISM Hyperspectral Imaging Data Over Glen Torridon, Gale Crater, Mars. In *Journal of Geophysical Research: Planets*. https://doi.org/10.1029/2021je007092

He, L., O'Sullivan, J.A., Politte, D.V., Powell, K.E., & Arvidson, R.E. (2019). Quantitative Reconstruction and Denoising Method HyBER for Hyperspectral Image Data and Its Application to CRISM. *IEEE Journal of Selected Topics in Applied Earth Observations and Remote Sensing*, *12*(4), 1219–1230. https://doi.org/10.1109/JSTARS.2019.2900644

Hintze, J.L., & Nelson, R.D. (1998). Violin Plots: A Box Plot-Density Trace Synergism. *The American Statistician*, *52*(2), 181–184. https://doi.org/10.1080/00031305.1998.10480559

Hiroi, T., & Pieters, C.M. (1994). Estimation of grain sizes and mixing ratios of fine powder mixtures of common geologic minerals. *Journal of Geophysical Research*, *99*(E5), 10867– 10879. https://doi.org/10.1029/94JE00841

Horgan, B.H.N., Cloutis, E.A., Mann, P., & Bell III, J.F. (2014). Near-infrared spectra of ferrous mineral mixtures and methods for their identification in planetary surface spectra. *Icarus*, *234*, 132–154. https://doi.org/10.1016/j.icarus.2014.02.031

Johnson, J.R., Bell III, J.F., Bender, S., Cloutis, E., Ehlmann, B., Fraeman, A., et al. (2018). Bagnold Dunes Campaign Phase 2: Visible/Near-Infrared Reflectance Spectroscopy of Longitudinal Ripple Sands. *Geophysical Research Letters*, *45*(18), 9480–9487. https://doi.org/10.1029/2018GL079025

Johnson, J.R., Grundy, W.M., Shepard, M.K. (2004). Visible/near-infrared spectrogoniometric observations and modeling of dust-coated rocks. *Icarus, 171*(2), 546-556. https://doi.org/10.1016/j.icarus.2004.05.013

Kokaly, R.F., Clark, R.N., Swayze, G.A., Livo, K.E., Hoefen, T.M., Pearson, N.C., et al. (2017). *USGS Spectral Library Version 7*. US Geological Survey. https://doi.org/https://doi.org/10.3133/ds1035

Kreisch, C.D., O'Sullivan, J.A., Arvidson, R.E., Politte, D.V., He, L., Stein, N.T., et al. (2017). Regularization of Mars Reconnaissance Orbiter CRISM

along-track oversampled hyperspectral imaging observations of Mars. *Icarus*, *282*, 136–151. https://doi.org/10.1016/j.icarus.2016.09.033

Lane, M.D., & Christensen, P.R. (2013). Determining olivine composition of basaltic dunes in Gale Crater, Mars, from orbit: Awaiting ground truth from Curiosity. *Geophysical Research Letters*, *40*(14), 3517–3521. https://doi.org/10.1002/grl.50621

Lapotre, M.G.A., Ehlmann, B.L., & Minson, S.E. (2017a). A probabilistic approach to remote compositional analysis of planetary surfaces. *Journal of Geophysical Research: Planets*, *122*(5), 983–1009. https://doi.org/10.1002/2016JE005248

Lapotre, M.G.A., Ehlmann, B.L., Minson, S.E., Arvidson, R.E., Ayoub, F., Fraeman, A.A., et al. (2017b). Compositional variations in sands of the Bagnold Dunes, Gale crater, Mars, from visible-shortwave infrared spectroscopy and comparison with ground truth from the Curiosity rover. *Journal of Geophysical Research: Planets*, *122*(12), 2489–2509. https://doi.org/10.1002/2016JE005133

Lapotre, M.G.A., Ewing, R.C., Weitz, C.M., Lewis, K.W., Lamb, M.P., Ehlmann, B.L., & Rubin, D.M. (2018). Morphologic Diversity of Martian Ripples: Implications for Large-Ripple Formation. *Geophysical Research Letters*, *45*(19), 10,229-10,239. https://doi.org/10.1029/2018GL079029

Lapotre, M.G.A., & Rampe, E.B. (2018). Curiosity's Investigation of the Bagnold Dunes, Gale Crater: Overview of the Two-Phase Scientific Campaign and Introduction to the Special Collection. *Geophysical Research Letters*, *45*(19), 10,200-10,210. https://doi.org/10.1029/2018GL079032

Lucey, P.G. (1998). Model near-infrared optical constants of olivine and pyroxene as a function of iron content. *Journal of Geophysical Research*, *103*(E1), 1703–1713.

Maki., J. (2014). MSL Mars Navigation Camera 5 RDR Mosaic V1.0 [Data Set]. NASA Planetary Data System. https://doi.org/https://doi.org/10.17189/1520335

Maki, J., Thiessen, D., Pourangi, A., Kobzeff, P., Litwin, T., Scherr, L., et al. (2012). The Mars Science Laboratory Engineering Cameras. *Space Science Reviews*, *170*(1–4), 77–93. https://doi.org/10.1007/s11214-012-9882-4

Malin, M.C. (2013a). MSL Mars Descent Imager 4 RDR Image V1.0 [Data Set]. NASA Planetary Data System. https://doi.org/https://doi.org/10.17189/1520349

Malin, M.C. (2013b). MSL Mars Mast Camera 4 RDR Image V1.0 [Data Set]. NASA Planetary Data System. https://doi.org/https://doi.org/10.17189/1520328

Malin, M.C., Ravine, M.A., Caplinger, M.A., Ghaemi, T.F., Schaffner, J.A., Maki, J.N., et al. (2017). The Mars Science Laboratory (MSL) Mast cameras and Descent imager: Investigation and Instrument Descriptions. *Earth and Space Science*, *4*(8), 506–539. https://doi.org/10.1002/2016EA000252

McEwen, A.S. (2005). MRO Mars High Resolution Image Science Experiment EDR V1.0 [Data Set]. NASA Planetary Data System. https://doi.org/https://doi.org/10.17189/1520179

McEwen, A.S., Eliason, E.M., Bergstrom, J.W., Bridges, N.T., Hansen, C.J., Delamere, W. et al. (2007). Mars reconnaissance orbiter's high resolution imaging science experiment (HiRISE). *Journal of Geophysical Research E: Planets*, *112*(5), 1–40. https://doi.org/10.1029/2005JE002605

McFadden, L.A., & Cline, T.P. (2005). Spectral reflectance of Martian meteorites: Spectral signatures as a template for locating source region on Mars. *Meteoritics and Planetary Science*, *40*(2), 151–172. https://doi.org/10.1111/j.1945-5100.2005.tb00372.x

McSween, H.Y., Ruff, S.W., Morris, R.V., Gellert, R., Klingelhöfer, G., Christensen, P.R., et al. (2008). Mineralogy of volcanic in Gusev Crater, Mars: Reconciling Mössbauer, Alpha Particle X-Ray Spectrometer, and Miniature Thermal Emission Spectrometer spectra. *Journal of Geophysical Research E: Planets*, *113*(6), 1–14. https://doi.org/10.1029/2007JE002970.

Milliken, R. (2020). RELAB Spectral Library Bundle [Data Set]. NASA Planetary Data System. https://doi.org/https://doi.org/10.17189/1519032

Moreland, E.L, Arvidson, R.E., Morris, R.V., Condus, T., Hughes, M.N., Weitz, C.M, & VanBommel, S.J. (2022). Orbital and In-Situ Investigation of the Bagnold Dunes and Sands of Forvie, Gale Crater, Mars [Data Set]. Digital Research Materials (Data & Supplemental files). 102. https://doi.org/10.7936/2jv6-c769

Murchie, S., Arvidson, R., Bedini, P., Beisser, K., Bibring, J. P., Bishop, J., et al. (2007). Compact Reconnaissance Imaging Spectrometer for Mars (CRISM) on Mars Reconnaissance Orbiter (MRO). *Journal of Geophysical Research E: Planets*, *112*(5), 1–57. https://doi.org/10.1029/2006JE002682

O'Connell-Cooper, C. D., Thompson, L. M., Spray, J. G., Berger, J. A., Gellert, R., McCraig, M., et al. (2022). Statistical analysis of APXS-derived chemistry of the clay-bearing Glen Torridon region and Mount Sharp group, Gale crater, Mars. Journal of Geophysical Research: Planets, 127, e2021JE007177. https://doi.org/10.1029/2021JE007177

Rampe, E.B., Blake, D.F., Bristow, T.F., Ming, D.W., Vaniman, D.T., Morris, R.V., et al. (2020). Mineralogy and geochemistry of sedimentary rocks and eolian sediments in Gale crater, Mars: A review after six Earth years of exploration with Curiosity. *Geochemistry*, *80*(2). https://doi.org/10.1016/j.chemer.2020.125605

Rampe, E.B., Lapotre, M.G.A., Bristow, T.F., Arvidson, R.E., Morris, R.V., Achilles, C.N., et al. (2018). Sand Mineralogy Within the Bagnold Dunes, Gale Crater, as Observed In Situ and From Orbit. *Geophysical Research Letters*, *45*(18), 9488–9497. https://doi.org/10.1029/2018GL079073

Rogers, A.D., & Bandfield, J.L. (2009). Mineralogical characterization of Mars Science Laboratory candidate landing sites from THEMIS and TES data. *Icarus*, *203*(2), 437–453. https://doi.org/10.1016/j.icarus.2009.04.020

Seelos, F. (2016). MRO CRISM Map-Projected Targeted Reduced Data Record V1.0. [Data Set] NASA Planetary Data System. https://doi.org/https://doi.org/10.17189/1519470

Seelos, K.D., Seelos, F.P., Viviano-Beck, C.E., Murchie, S.L., Arvidson, R.E., Ehlmann, B.L., & Fraeman, A.A. (2014). Mineralogy of the MSL Curiosity landing site in Gale crater as observed by MRO/CRISM. *Geophysical Research Letters*, *41*(14), 4880–4887. https://doi.org/10.1002/2014GL060310

Silvestro, S., Vaz, D.A., Ewing, R.C., Rossi, A.P., Fenton, L.K., Michaels, T.I., et al. (2013). Pervasive aeolian activity along rover Curiosity's traverse in Gale Crater, Mars. *Geology*, *41*(4), 483–486. https://doi.org/10.1130/G34162.1

Stamnes, K., Tsay, S.C., Wiscombe, W., & Jayaweera, K. (1988). Numerically stable algorithm for discrete-ordinate-method radiative transfer in multiple scattering and emitting layered media. *Applied Optics*, *27*(12), 2502. https://doi.org/10.1364/ao.27.002502

Stein, N.T., Arvidson, R.E., O'Sullivan, J.A., Catalano, J.G., Guinness, E.A., Politte, DV., et al. (2018). Retrieval of Compositional End-Members From Mars Exploration Rover Opportunity Observations in a Soil-Filled Fracture in Marathon Valley, Endeavour Crater Rim. *Journal of Geophysical Research: Planets*, *123*(1), 278–290. https://doi.org/10.1002/2017JE005339

Sullivan, R., Baker, M., Newman, C., Turner, M., Schieber, J., Weitz, C., et al. (2022). The Aeolian Environment in Glen Torridon, Gale Crater, Mars. *Journal of Geophysical Research*, submitted.

Sunshine, J.M., & Pieters, C.M. (1998). Determining the composition of olivine from reflectance spectroscopy. *Journal of Geophysical Research*, *103*(E6), 13675-13688. https://doi.org/10.1029/98JE01217

Trang, D., Lucey, P.G., Gillis-Davis, J.J., Cahill, J.T.S., Klima, R.L., & Isaacson, P.J. (2013). Near-infrared optical constants of naturally occurring olivine and synthetic pyroxene as a function of mineral composition. *Journal of Geophysical Research: Planets*, *118*(4), 708–732. https://doi.org/10.1002/jgre.20072

Vanbommel, S.J., Gellert, R., Arvidson, R.E., Berger, J.A., Boyd, N.I., McCraig, M., et al. (2020). Quantification of Volatile Elements through Spectral Modeling and Analyses of APXS Data: Comparing Murray and Sheepbed. *51st Lunar and Planetary Science* Conference, No. 1452.

Vanbommel, S.J., Gellert, R., Berger, J.A., Campbell, J.L., Thompson, L.M., Edgett, K.S., et al. (2016). Deconvolution of distinct lithology chemistry through oversampling with the Mars Science Laboratory Alpha Particle X-Ray Spectrometer. *X-Ray Spectrometry*, *45*(3), 155–161. https://doi.org/10.1002/xrs.2681

VanBommel, S.J., Gellert, R., Berger, J.A., Thompson, L.M., Edgett, K.S., McBride, M.J., et al. (2017). Modeling and mitigation of sample relief effects applied to chemistry measurements by the Mars Science Laboratory Alpha Particle X-ray Spectrometer. *X-Ray Spectrometry*, *46*(4), 229–236. https://doi.org/10.1002/xrs.2755

VanBommel, S.J., Gellert, R., Berger, J.A., Yen, A.S., & Boyd, N.I. (2019a). Mars Science Laboratory Alpha Particle X-ray spectrometer trace elements: Situational sensitivity to Co, Ni, Cu, Zn, Ga, Ge, and Br. *Acta Astronautica*, *165*(11), 32–42. https://doi.org/10.1016/j.actaastro.2019.08.026

VanBommel, S.J., Gellert, R., Boyd, N.I., & Hanania, J.U. (2019b). Empirical simulations for further characterization of the Mars Science Laboratory Alpha Particle X-ray Spectrometer: An introduction to the ACES program. *Nuclear Instruments and Methods in Physics Research, Section B: Beam Interactions with Materials and Atoms*, *441*(E7), 79–87. https://doi.org/10.1016/j.nimb.2018.12.040

Vasavada, A.R., Grotzinger, J.P., Arvidson, R.E., Calef, F.J., Crisp, J.A., Gupta, S., et al. (2014). Overview of the Mars Science Laboratory mission: Bradbury Landing to Yellowknife Bay and beyond. *Journal of Geophysical Research: Planets*, *119*, 1134–1161. https://doi.org/10.1002/2014JE004622

Weitz, C.M., Connell, C.O.C., Thompson, L., Sullivan, R.J., Baker, M., & Grant, J.A. (2022). The Physical Properties and Geochemistry of Grains on Aeolian Bedforms at Gale Crater, Mars. *Journal of Geophysical Research: Planets*, submitted.

Weitz, C.M., Sullivan, R.J., Lapotre, M.G.A., Rowland, S.K., Grant, J.A., Baker, M., & Yingst, R.A. (2018). Sand Grain Sizes and Shapes in Eolian Bedforms at Gale Crater, Mars. *Geophysical Research Letters*, *45*(18), 9471–9479. https://doi.org/10.1029/2018GL078972

Wolff, M.J., Smith, M.D., Clancy, R.T., Arvidson, R., Kahre, M., Seelos IV, F., et al. (2009). Wavelength dependence of dust aerosol single scattering albedo as observed by the compact reconnaissance imaging spectrometer. *Journal of Geophysical Research, 114*(E00D04). https://doi.org/10.1029/2009JE003350